UNIVERSITY OF TWENTE.

Faculty of Science and Technology,
Biomedical Engineering

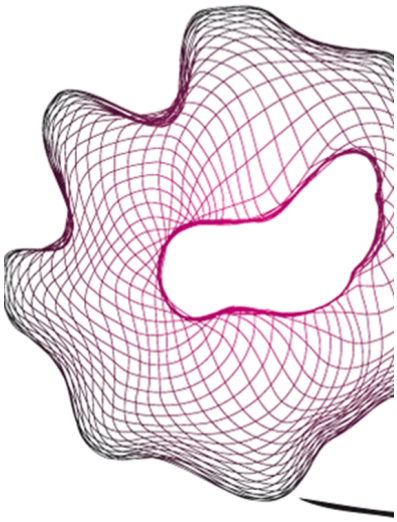

Improving the diagnosis of crystals in synovial fluid by combining Raman spectroscopy with polarized light microscopy

Charline Kuipers
s2016141

Master thesis
November 3, 2020

Supervisor:
dr. C. Otto

Univeristy of Twente
Medical cell biophysics
VieCurie Medical center, Venlo
The Netherlands

Author:

Name:	Charline Kuipers
Student number:	s2016141
Education:	Biomedical engineering - BioEngineering Technologies
Institution:	University of Twente
Group:	Medical cell biophysics, Viecuri medical center

Committee members:

Supervisor:	dr. Cees Otto
Committee chair:	dr. Cees Otto
Member other research group:	dr. ir. Nienke Bosschaart
External advisor:	dr. Matthijs Janssen, Rheumatologist
Committee member:	Prof. dr. Leon Terstappen, MD
Committee member:	dr. ir. Agustin Enciso Martinez

Abstract

Crystalline arthritides are characterised by the deposition of crystals in synovial fluid (SF). Gout is the most common form and presents itself with the deposition of monosodium urate crystals. Calcium pyrophosphate dihydrate (CPPD) deposition disease is identified by calcium pyrophosphate crystals in the synovial fluid. Other less common crystals that are found in synovial fluid are calcium oxalate monohydrate and dihydrate, hydroxyapatite, cholesterol and residues of intra-articular corticosteroids which are used to treat symptoms that are caused by crystal deposition. The current method to identify crystals in synovial fluid is compensated polarized light microscopy (CPLM). This technique is often only available in specialised areas and the sensitivity and specificity are affected by user experience. Additionally, not all crystals are equally visible under CPLM due to varying degrees of birefringence. Raman spectroscopy could be a method to improve the identification of crystals because it can provide detailed information about the chemical structure of molecules. In this study, Raman spectroscopy was combined with polarization microscopy to improve the identification of crystals in SF. Additionally, a platform was built to identify newly measured crystals by using a database and correlating the measurements with the database. 195 birefringent objects were measured and 18 Raman spectra were placed in the database for correlation. 101 measurements were correctly identified with varying correlation strengths by using correlation-based crystal identification. Additionally, different sub-types of CPPD were identified and calcium carbonate crystals in the form of calcite and aragonite were possibly found which have rarely been mentioned in literature in combination with SF. The corticosteroid Kenacort was also detected by using the database which is normally challenging to distinguish from CPPD crystals. In conclusion, this study showed that combining Raman spectroscopy with polarization microscopy can provide much new, valuable information. It was also shown that crystal detection is possible by correlating new Raman measurements with a database of known components. Optimisation for different aspects such as data processing and synovial fluid sample preparation are still required but this study has provided a foundation to work toward an improved diagnosis of crystals in SF by combining Raman spectroscopy and polarization microscopy.

Contents

1 Introduction

Synovial fluid (SF) functions as a biological lubricant for joint surfaces and allows passing of nutrients and regulatory cytokines. The visco-elastic fluid fills the cavity between two articulating bones and provides low-friction and low-wear properties. SF is an ultrafiltrate of blood plasma to which hyaluronic acid and lubricin are added by synoviocytes. The typical hyaluronic acid concentration in human SF varies between 1 and 4 mg/ml and decreases with age. It is suggested that this might contribute to age related detoriation of knee articular cartilage [1]. SF is further composed of water, proteins, proteoglycans, glycosaminoglycans (GAGs), lipids, small inorganic salts, and metabolites [2]. Healthy SF is transparent, viscous, colourless and present in low amounts. Changes in these properties can be of great value when diagnosing joint diseases [3]. In the Netherlands, one in nine people suffer from a rheumatic disease. While the chances of early mortality due to rheumatic diseases are not or barely increased, the quality of life can be severely affected. Patients with rheumatic diseases experience pain, loss of mobility, and restrictions in their physical functioning and daily activities. Several symptoms for these diseases are similar and include one or more painful, swollen joints. If the condition remains untreated this leads to impairment and eventually disability. In 2011, healthcare costs for rheumatic patients in the Netherlands were 1.9 billion euros and it is expected that these costs will rise up to 3.7 billion euro in 2030 because of the ageing population [4]. Rheumatic disease describes a wide range of diseases with four main groups: osteoarthritis, rheumatoid arthritis, gout and osteoporosis. Osteoarthritis (OA) is by far the most common rheumatic disease and accounts for 64% of the patients. OA is characterised by the breakdown of joint cartilage and can be caused by wear-and-tear or injury. Rheumatoid arthritis (RA) is a chronic inflammatory disease that can damage all organs rather than just the joints. RA affects the joint lining and cartilage and can lead to severe bone erosion and joint deformity. Gout is a form of crystalline arthritis and is characterised by deposition of monosodium urate (MSU) crystals in the synovial fluid and affects approximately 19% of all rheumatic disease patients. In addition to MSU, a number of other crystals can be found in the SF due to different metabolic changes. Because many pathologies that involve crystal deposition in SF are represented by a similar clinical picture, it can be challenging to correctly identify different crystals and to connect these to different metabolic changes. For several decades, the gold standard for identification of gout and other crystals in SF has been compensated polarized light microscopy (CPLM). This technique is often only available in specialised areas and the sensitivity and specificity are affected by user experience. Additionally, not all crystals are equally visible under CPLM due to varying degrees of birefringence [5]. This research aims to improve current diagnostic methods that are used for crystalline arthritides such as gout by introducing Raman spectroscopy to the currently used polarized light microscopy. Raman spectroscopy relies on inelastic light scattering and is used to identify vibrational modes of molecules and provides a molecular fingerprint of a substance. It is expected that Raman spectroscopy will complement polarization microscopy to increase crystal identification.

1.1 Crystals in synovial fluid

Crystalline arthritis is a general classification for the accumulation and deposition of different crystals in one or more joints and specifically in SF which can cause acute inflammatory responses. In the following sections, different crystals that have been observed will be discussed in detail.

1.1.1 Monosodium urate

Gout is caused by the deposition of monosodium urate (MSU) crystals in synovial tissues which leads to highly inflammatory responses or "gout flares". Aggregates of MSU crystals can cause chronic inflammation that can lead to structural joint damage. The most affected joint in gout patients is the first metatarsophalangeal joint. Gout can be divided in four clinical phases; asymptomatic hyperuricemia, acute gouty arthritis, intercritical gout and chronic tophaceous gout [6]. Gout can, in contrast to other arthritic conditions, essentially be cured by lowering serum urate levels to prevent further crystal formation [7]. Gout is generally seen in men between the ages of 30 to 45 and women over 55. Additionally, a number of comorbid conditions are identified for gout such as renal disease, hypertension, diabetis mellitus and cardiovascular diseases. Some of these comorbidities, such as renal failure, might be causing gout whereas other comorbidities, such as hypertension, are speculated to be caused by high uric acid levels or gout [8]. MSU crystals are formed when serum urate levels are elevated. Urate is one of the end products of purine metabolism. Hyperuricemia happens when MSU is above the saturation point, which increases the risk of crystal formation. However, only a small portion of hyperuricemic patients develop gout. This already indicates a complex relationship between serum urate levels and MSU crystal formation. Hyperuricemia can have different causes [9]. The primary risk factor is the general absence of urate oxidase in humans. Urate oxidase breaks down uric acid to the more soluble allantoin in other mammals. Generally, the absence of urate expression in humans and other primates is seen as an advantage, considering the high antioxidant properties of uric acid [10]. Unfortunately, this does result in a higher risk for developing uric acid-related diseases. The absence of this gene alone is not enough to induce hyperuricemia. Other contributers include purine rich diets, renal underexcretion of urate, patients that take diuretic medications, and conditions with excessive cell and purine turnover. When MSU crystals are formed, they activate resident tissue macrophages which secrete different inflammatory cytokines. From here, a neutrophilic influx is triggered that further initiates the production of pro-inflammatory mediators. The growth mechanisms of MSU crystals remains mostly unknown. Through an optical microscope, MSU crystals are needle shaped with a triclinic structure with three unequal axes all not perpendicular to each other. On a molecular scale, the long axis is made of sheets from closely-spaced purine rings that are stacked on top of each other. The purine rings each contain closely aligned urate anions and water molecules that are bonded by hydrogen bonding. The water molecules are held in place by two sodium ions and a hydrogen bond to the purine ring. In general crystallization processes, three key elements are required to initiate crystal formation. The first is a reduced solubility,

which leads to supersaturation, followed by nucleation. In nucleation clusters of solute molecules are formed that eventually reach a critical size before stabilizing. The last element is crystal growth. If crystals have already formed, it is likely that more crystals will form faster [9]. A systematic literature review [11] found that the most consistent factor involved in MSU crystal formation were elevated urate concentrations. Factors that were found to be important for controlling urate solubility were temperature, pH levels and sodium ions. Gout is diagnosed by aspiration of SF and identifying MSU crystals under a polarized light microscope where the crystals are needle shaped and show a negative birefringence. Patients can be treated with systematic doses of allopurinol to decrease serum urate levels and intra-articular corticosteroid injections such as triamcinolonacetonide and methylprednisolon to alleviate pain [12].

1.1.2 Calcium pyrophosphate dihydrate

Calcium pyrophosphate dihydrate (CPPD) deposition disease is another arthropathy that involves crystal deposition in synovial and periarticular tissues. An estimated 1% of the Dutch population is affected by CPPD deposition disease and it occurs twice as often in women as it does in men [13]. Pyrophosphate is a metabolic byproduct of many intracellular processes found in most cells, and can also be produced extracellularly. Pyrophosphate is involved in the healthy functioning of connective tissues such as bones and joints. In excess however, pyrophosphate can form complexes with calcium and form microscopic calcium pyrophosphate (CPP) crystals causing different complications [14]. CPPD describes a broad range of pathologies that involve the deposition of calcium pyrophosphate crystals which can range from asymptomatic to chronic inflammatory arthritis. CPPD mostly occurs in elderly patients with over 50% of the patients older than 84 years [15]. Acute CPPD crystal arthritis presents itself in acute flares that result in joint pain, swelling, warmth and function loss. An attack can last several days to weeks and is mostly seen in the knee but can also be found in other load-bearing joints. Acute CPPD was previously known as pseudogout because the clinical picture was very similar to gout. The cause of CPPD can vary greatly and the disease is also associated with a number of comorbidities, some of which are also rheumatic [16]. CPPD crystals have been found in combination with rheumatoid arthritis, psoriatic arthritis, different inflammatory arthritides, septic arthritis and gout [17]. It has been estimated that patients with osteoarthritis (OA) are almost three times more likely to develop CPPD. Acute CPPD flares can be caused by severe joint trauma, surgery and genetics. Some people inherit a predisposition to CPPD crystal deposition which makes them more susceptible for developing acute CPPD crystal arthritis. Additionally, a genetic disorder hemochromatosis, where excess iron is stored in the body, has been linked with an increased risk for acute CPPD crystal arthritis possible because of the inhibitory activity of iron on pyrophosphatases. Other metabolic diseases that have been linked to acute CPPD crystal arthritis are hyperparathyroidism, hypophosphatasia [18], hypomagnesemia [19] and a kidney disorder called Gitelman syndrome [20][21].

CPPD is diagnosed by clinical presentation and the presence of CPPD crystals in the SF viewed under CPLM. Both monoclinic (m-CPPD) and triclinic (t-CPPD) crystals can occur in SF. m-CPPD crystals are generally elongated, rod-like shaped whereas t-CPPD crystals are more rhomboid or cuboid [22]. It has been suggested that m-CPPD induces a stronger inflammatory response than t-CPPD when measuring exudate volumes, leukocyte counts, protease activity and prostaglandin E_2 [23]. Under CPLM, CPPD crystals show a weak positive birefringence. Unfortunately, a great variation exists between laboratories in their capability of recognising CPPD crystals [24].

In contrast to gout, acute CPPD cannot be cured. Therapies are aimed at pain management which include resting, joint aspiration and intra-articular glucocorticosteroid injections. Non-steroidal anti-inflammatory drugs (NSAIDs) and low-dose oral colchicine are effective but their use is limited by toxicity and co-morbidities which are especially relevant given the average age of the patients. Unfortunately, these treatments are less successful in chronic forms of CPPD and there currently is no treatment option that can modify the disease or stop CPPD crystal formation [25].

1.1.3 Calcium oxalate

Less commonly occurring crystals in SF are calcium oxalate crystals in monohydrate or dihydrate form. These crystals can appear with MSU and CPPD crystals or alone. and are typically seen in patients with hyperoxaluria. Hyperoxaluria can be caused by a genetic disorder, or an increased intestinal absorption of dietary oxalate. Oxalate is a natural product of the metabolism or it can be ingested via an oxalate rich diet which includes peanuts, spinach and sweet potatoes. Oxalate is excreted through the renal system. Excessive oxalate in the urinary tract can damage the kidneys by limiting the renal excretion. Many patients therefore also suffer from renal failure. Increased oxalate in tubular fluid can lead the anion to form insoluble complexes with calcium which can lead to crystal or kidney stone formation. Kidney stones are largely made from calcium oxalate monohydrate (COM) or dihydrate (COD). It is important to distinguish between both because the latter appears to respond better to treatments such as shock wave lithotripsy (SWL) [26]. Calcium oxalate crystals can deposit in various tissues in the body, which can induce inflammatory responses that cause abnormal accumulation of fluid in the joints. Both COM and COD crystals are almost indistinguishable under CPLM from other crystals such as CPPD and MSU. COM crystals are shaped as irregular squares or rods, making them similar to CPPD crystals. COD crystals have a more distinguishable envelope shape. Both crystals have a weak positive birefringence like CPPD crystals. Like gout and acute CPPD, the treatment for oxalate arthritis is mostly focused on pain relief with NSAIDs, colchicine and steroids. However, because most patients with oxalate arthritis often also suffer from renal diseases, the use of NSAIDs is limited. Therapy for oxalate arthritis should thus be focused on the underlying medical disease. Patients with hyperoxaluria may benefit from therapies that lower oxalate precipitation in tissues and urine through hydration and crystalline inhibitors such as oral phosphorus and citrate salts [27].

1.1.4 Hydroxyapatite deposition disease

Hydroxyapatite is an essential mineral of normal bone and teeth. Dry bone weight is for 70% made from hydroxyapatite as the inorganic component and the enamel of teeth is almost completely made from hydroxyapatite. Hydroxyapatite depositional disease (HADD) describes a wide range of abnormalities that involve hydroxyapatite, including hydroxyapatite-induced arthritis which is caused by calcium hydroxyapatite crystals. When hydroxyapatite crystals deposit in soft tissues, an inflammatory reaction is induced. The presence of hydroxyapatite crystals can give rise to acute inflammation of tendons, intervertebral discs, joint capsules, synovium and cartilage. However patients can also be asymptomatic [28]. The most affected joint is the shoulder causing "Milwaukee shoulder" which leads to a destructive shoulder arthropathy.

While the pathogenesis of HADD is mostly unknown, a possible mechanism is fibrocartilage, which is a transitional tissue between hyaline cartilage and and dense regular connective tissue, formation triggered by local hypoxia which leads to calcium deposition and vascular proliferation. Then, calcium is deposited in the degenerated area and can gradually progress through the tendon or ligament [29]. Additionally, a process similar to endochondral ossification has been suggested as a pathologic pathway together with erroneous differentiation of tendon-derived stem cells into calcium depositing chondrocytes or osteoblasts [30]. The pathophysiology of mobilizing hydroxyapatite crystals is also unknown. Several suggestions have been made which include, tendon damage, decreased vascularity with pre-existing tissue degeneration, local necrosis and metabolic disturbances. It is thought that any traumatic event can encourage hydroxyapatite deposition through the fibrogenic healing cascade and deposition of extracellular matrix [31]. Controversy exists about whether hydroxyapatite crystals are the primary cause of arthritic symptoms or a secondary cause of joint damage [32].

Calcium hydroxyapatite crystals are difficult to diagnose with conventional microscopes because of their small size (75-250 nm) and the absence of birefringence in polarized light. Correctly identifying these crystals currently requires electron microscopic radioisotropic techniques or X-ray diffraction analysis. HADD usually resolves spontaneously within four weeks, however the disease can also become chronic. The treatment for HADD is focused on pain relief by using NSAIDs, physiotherapy, intra-articular corticosteroid injections and in some cases surgery to remove calcifications [33].

1.1.5 Cholesterol

Cholesterol is a lipid that is an essential component of all cellular membranes. Cholesterol is important for membrane structure and functioning and is involved in the maintenance of membrane permeability and cell signalling. Occasionally, cholesterol crystals are found in soft tissues such as the joint and tendons. The crystals are often found in patients with rheumathoid arthritis (RA), osteoarthritis (OA) and gout. Cholesterol crystals are a secondary symptom of several rheumatic diseases as they are thought to appear in SF because of local factors such as increased production or defective

metabolism of cholesterol in the synovial membrane, increased synovial membrane permeability and intra-articular bleeding. Additionally, a systemic cause for cholesterol crystals in RA patients can also be hyperlipoproteinemia [34]. Under a polarized light microscope, cholesterol crystals can be characterised by their distinctive large broad plate shape with notched corners. The crystals can show positive and negative birefringence in varying degrees depending on the crystal orientation [35]. Cholesterol crystals are also associated with atherosclerosis and renal diseases. The inflammatory role of cholesterol crystals in SF is not discussed extensively in literature. Several case studies suggest that these crystals do not contribute to symptomatic disease and it is thought that the presence of cholesterol crystals are more a rare consequence rather than a pathogenic factor [36]. However, it is known that cholesterol crystals can activate NLRP3 inflammasome in macrophages which is notably the same inflammasome that is thought to trigger arthritic symptoms in gout and acute CPPD by triggering the release of pro-inflammatory cytokines such as IL-1β and IL-18 [32]. These conflicting suggestions already indicate that more insight is required in the pathology and comorbidities of the presence of cholesterol crystals.

1.1.6 Maltese crosses

SF of patients with acute monoarticular arthritis can sometimes contain maltese cross spherules. These spherules are rare but are strongly associated with pain and fever. Under polarized light microscopy these crystals show a strong positive birefringence. It was long thought that these crosses were mainly composed of lipids [37][38], however, one study [39] used Raman spectroscopy in an attempt to determine the chemical composition of maltese cross spherules and found that they are likely composed of calcium carbonate rather than phospholipids or basic calcium phosphates. To understand the pathogenesis of these crosses, their chemical composition should first be determined.

1.1.7 Intra-articular corticosteroids

For several types of arthritides, including crystalline forms, intra-articular corticosteroid injections are used for symptom relief and management [40]. Corticosteroid injections can be water-soluble but water-insoluble corticosteroid esters are most commonly used for intra-articular injections. This can lead to microcrystalline aggregates which can induce post-injection flares that result in a localized inflammatory response. Commonly used steroids are hydrocortisone, cortisone, dexamethasone, triamcinolone (KenaCort®) and methylprednisolone (DepoMedrol®) and all these have been found in association with a post-injection inflammatory response [41].

When viewing the crystals under polarized light microscopy, they can be positively and negatively birefringent in different degrees [42]. Although these crystals can be present in SF for a considerable time post-injection, they are not mistaken for other pathologies, however they can obstruct the microscopic view and make a diagnosis more challenging [43].

1.1.8 Crystal birefringence

Crystals consist of highly ordered and repetitive atomic structures. They can be isotropic or anisotropic. Isotropic crystals are directionally independent thus their physical properties are independent of their orientation. The interaction with light is constant along all axes therefore, when light enters an isotropic crystal, it refracts at a constant angle and propagates through the crystal with a single velocity. Anisotropic crystals have crystallographic distinct axes and therefore their optical properties are dependent on their orientation. When light enters on the optical axis of the crystal, the behaviour is similar to isotropic crystals and passes with a constant velocity. However, when light enters a non-equivalent axis, it is split into two different polarized rays that are mutually perpendicular. This property is called birefringence and is seen in all anisotropic crystals in varying degrees. One of the polarized rays is directed perpendicular to the optical axis and is termed the ordinary ray. The refractive index of an ordinary ray is constant, and the propagation velocity is not dependent on the propagation direction. The propagation velocity of the ordinary wave is given by the ordinary refractive index n_o. The direction of the second ray, termed extraordinary ray, is oriented in the direction of the optical axis. Here, the propagation velocity and the refractive index n_e are dependent on the propagation direction of the ray within the crystal.

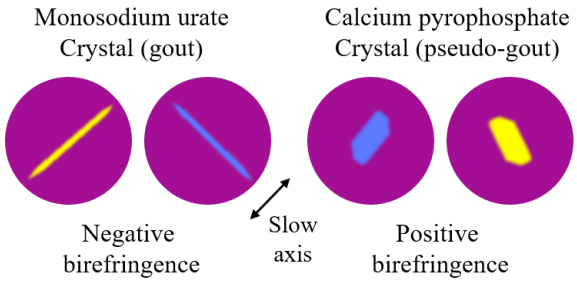

Figure 1: Example of positive and negative birefringence in MSU crystals and CPPD crystals under compensated polarized light microscopy (adapted from[44])

The largest difference between the refractive indexes of the ordinary and extraordinary waves is the birefringence, $d_n = n_e - n_o$. A crystal can be positively or negatively birefringent. For positive birefringent materials $n_e > n_o$, and negative birefringent materials $n_e < n_o$. The ray with the highest refractive index is known as the slow ray. MSU crystals are negatively birefringent. Under compensated polarized light microscopy, this results in a yellow interference colour when the long axis of the crystal is oriented parallel to the slow axis of the first order retardation plate (see figure 1). When the crystal rotates 90 degrees the interference colour becomes blue. CPPD crystals are positively birefringent and here, the interference colours are opposite to MSU crystals. All other previously mentioned crystals and their microscopic and birefringent properties are summarised in table 1.

Table 1: Overview of crystals found in SF and their birefringent properties

Crystal type	Microscopic view	Birefringence
Monosodium urate	Needle	Strong negative
Calcium pyrophosphate	Rhomboid	Weak positive
Calcium oxalate monohydrate	Rhomboid	Variable positive
Calcium oxalate dihydrate	Envelope	Variable positive
Cholesterol	Broad plates with notched corners	Strong negative
Hydroxyapatite	Hexagonal	No (Alazarin red stain)
Maltese cross	Maltese cross	Strong positive
Intra-articular corticosteroids [45]	Irregular	Strong positive & negative

1.2 Polarized light microscopy

Light waves are electromagnetic waves where the magnetic field points at a right angle to the electric field. Polarized light is light where the electric field is only oscillating in one direction. A polarizer only lets light through in one orientation. A polarized light microscope is used to observe and capture specimens that are mainly visible through their optically anisotropic character. In a polarized light microscope, two polarizing filters are commonly used. The first is placed between the light source and the birefringent specimen which results in plane polarized light. The second polarizing filter, or analyser, is placed in the optical pathway between the objective rear aperture and the camera port. This is shown in figure 2. The contrast of the image comes from the interaction between plane polarized light with a birefringent crystal that produces two individual polarized wave components in mutually perpendicular waves. It can be challenging to correctly identify different crystals because of many similarities and a lack of parameters to distinguish the crystals. A more specific method is necessary to unequivocally characterise a crystal. Raman spectroscopy can provide a solution.

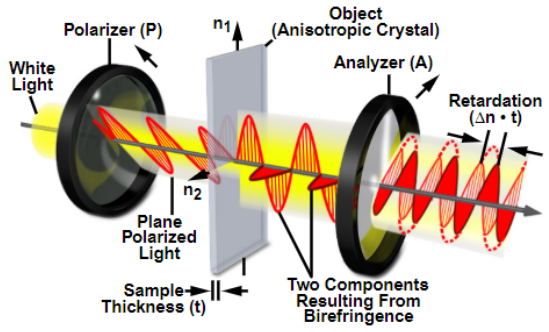

Figure 2: Light path from light source through birefringent sample with polarizing filters [44]

1.3 Raman spectroscopy

Raman spectroscopy is based on inelastic scattering of photons. Interactions between electrons in a molecule and the electric field of the electromagnetic radiation are what cause the Raman effect. Because of this interaction, the polarizability of a molecule changes which induces a temporary dipole moment that oscillates with the frequency of the incident electric field of the electromagnetic radiation. The polarizability of a molecule is affected by the vibrational modes of a molecule which is what gives Raman spectroscopy its molecular specificity [46].

An quantum-mechanical description of the Raman effect can be found in figure 3. The energy levels are separated by an energy quantum $\Delta E = hv_m$ with Planck's constant h and the molecular vibration frequency v_m. When photons with energy hv_0 interact with a molecule with discrete energy levels, elastic collision scatter photons of the same energy which is called Rayleigh scattering. This accounts for most of the light scattered by molecules. Inelastic collisions scatter photons of smaller (Stokes Raman scattering) or higher (anti-Stokes Raman scattering) energies. Stokes Raman scattering is more likely to occur than anti-Stokes Raman scattering because most molecules are in their vibrational ground state at room temperature [47].

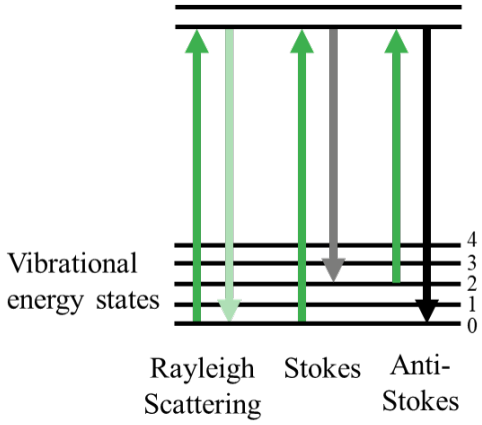

Figure 3: Principle of Raman spectroscopy based on vibrational energy states.

Vibrational modes that are exhibited by a molecule, contribute to the polarizability of the molecule. Therefore, the induced dipole moment and the amplitude of the emitted light are modulated by the frequency of the molecular vibration. The oscillating charges make the molecule scatter light with different frequency components which a spectrometer can analyse and translate into a Raman spectrum. A Raman spectrum is composed of the light intensity plotted against the vibrational frequency expressed in wavenumbers which are expressed as $\tilde{v} = \frac{1}{\lambda}$ in cm^{-1}. Frequencies correspond to the energy levels of different molecular vibrations and are independent from the wavelength of the light source. A spectrum has one or more bands which reflect the vibrational energies of the molecules within the analysed sample which are related to the nature of bonding. Main molecular vibrations include stretching and bending modes where frequencies of stretching modes are generally higher than bending frequencies [48].

Raman spectroscopy has been applied to analyse MSU and CPPD crystals [49] [50]. While MSU and CPPD crystal spectra are well defined in literature, there is a lack of literature about the remaining, previously described crystals. Table 2 shows an overview of these crystals and their expected Raman bands. Different studies have shown that Raman spectroscopy can identify different crystals in SF [49][51]. A prototype was even developed that would detect MSU crystals noninvasively around the first metatarsophalangeal joint [50]. The study used four patients that were diagnosed with gout and the Raman set-up used a 785 nm laser with a maximum power of 100 mW. Unfortunately, the device was not optimal for the clinic because of its weight and impractical patient handling where patients needed to be placed in an exact position before the measurement could be performed.

Another group developed a protocol to improve crystal extraction to target crystals more easily and downsized the Raman set-up to the size of a shoebox to make it more clinically applicable [52]. The group developed an enzymatic digestion treatment of synovial fluid that was followed by a customised filtration process that collected crystals over a sub-millimeter sized spot. This process made it possible to remove organic debris and centralise all crystals within one spot without harming the crystals.

They found that their system was superior to CPLM in detecting CPPD crystals but the opposite was true for MSU crystals. This difference was noticed especially in SF samples with low concentrations of crystals. Their Raman spectroscopy system was not able to detect crystals below a threshold of 0.1 μg/ml whereas CPLM can detect even a single crystal in a sample because of the strong birefringence of the MSU crystals. The paper argues that CPPD detection is higher with Raman spectroscopy because of the crystals low birefringence but strong characteristic Raman signal [53]. It can be suggested to combine both methods to improve the current diagnostics.

Table 2: Overview of crystals found in SF and their expected Raman bands found in literature. * main peaks

Crystal type	**Chemical formula**	**Expected Raman bands (cm^{-1})**
Monosodium urate [51]	$C_5H_3N_4NaO_3$	490, 590, 631*, 680, 749, 788, 875, 1012, 1063, 1128 1208, 1274, 1338, 1367, 1418 1447, 1500, 1600
Calcium pyrophosphate [54]	$Ca_2P_2O_7$	438, 498, 515, 535, 560, 592, 754, 915, 1050*, 1079, 1119, 1182
Calcium oxalate monohydrate [55]	$C_2CaO_4 \cdot H_2O$	508, 892, 1406, 1463, 1490, 1629
Calcium oxalate dihydrate [55]	$C_2CaO_4 \cdot 2\,H_2O$	504, 910, 1413, 1476, 1626
Cholesterol [56]	$C_{27}H_{46}O$	605, 700, 1440, 1467, 1670, 2864, 2930
Hydroxyapatite [57]	$Ca_{10}(PO_4)_6OH_2$	960

Extensive sample preparation of SF can be a limiting factor in a clinical setting where the sample is analysed immediately. In the current clinical situation, SF is obtained from the patient and immediately analysed with polarized light microscopy to provide an instant diagnosis, the whole process taking approximately ten minutes. This process should not be slowed down by extensive sample preparation steps and therefore, it must be possible to use Raman spectroscopy in the same, or comparable, manner. This study aims to integrate Raman spectroscopy into the currently used polarized light microscopy set-up to improve diagnostic outcome without compromising on the current diagnosis time. Additionally, a platform will be created that will make it possible to quickly identify newly measured crystals in SF by using a database and correlating the measurements with the database. With this goal in mind, different questions arise that will be answered during the course of this study. These questions include, but are not limited to:

- What is the most ideal sample preparation?
- Will all crystals be visible with the home-built microscope set-up?
- How can polarization be added to the current in-house Raman system for optimal polarized signal?
- Which components will be found next to the components previously described?
- How should the collected data be handled to build previously mentioned platform?
- Which factors in the data affect the correlation?
- What is the ideal clinical situation and which steps still need to be considered to reach this?

2 Materials and methods

This project was part of an ongoing collaboration between the medical cell biophysics group from the University of Twente and Viecuri hospital located in Venlo, the Netherlands. All patient material was provided by VieCuri hospital. VieCuri provided SF, aspirated with a needle derived from different joints, kidney stones and different corticosteroids for measurements. The samples were derived from both male and female patients in varying age groups and different pathologies. The samples were stored at room temperature for different periods of time.

2.1 Sample preparation

A total of 22 patient samples were used of which 20 where SF and two where kidney stones and a total of 313 birefringent object where measured of which 235 were measured in this study and 78 in a previous study. 213 measurements were eventually used in this study. Two kidney stones from two patients were measured to obtain COM and COD spectra. In addition to patient samples, synthetic crystals and corticosteroids were measured as control samples. MSU and CPPD crystals (InvivoGen) were measured as well as cholesterol, COM and hydroxyapatite (Sigma Aldrich) in crystal powder form and the corticosteroids methylprednisolonacetate (Depo Medrol®40 mg/ml) and triamcinolonacetonide (Kenacort®, 40 mg/ml) which were in liquid form. Lastly, polymeric hyaluronic acid, which is a major compound in SF, was measured in both low (27kDa) and high (2.0-2.2 MDa) molecular weight (Mw) solutions dissolved in 12.5 and 1.5 mg/ml PBS respectively with repeating units (disaccharide $C_{14}H_{21}NaNO_{11}$) of 402.31 g/mol. All samples where labelled with the indications received from the Rheumathologists to compare the indication with the findings from the Raman measurements. Samples of which the diagnosis was not provided where labelled as unknown.

SF was measured by directly placing a drop between 20-40 μl on a microscope slide (BMS, 12290). The sample was placed on the slide either by pipetting or directly from the syringe it was stored in which was dependent on how the sample was delivered. The drop was then covered with a 24x50 mm cover glass (VWR, 631-0158). The sample was dispersed over the microscope slide, covering the entire area under the cover glass. It sometimes occurred that components in the sample, including crystals, would still be floating, which made it difficult to measure with Raman. In this case, the sample was left to dry for approximately 30 min so that most components would settle. The time to find a birefringent object varied between samples. In some cases, birefringent objects could be found within one minute whereas in other samples it could that up to ten minutes to find birefringent object.

The kidney stones where measured in pulverized form. One kidney stone was already pulverized and the other kidney stone ($\pm$ 1 cm by 0.5 cm) was pulverized with a hammer. Tiny fractions of the pulverized kidney stones were measured and also placed on a microscope slide and covered with a cover glass to protect the microscope objective. Areas were selected where the fragments of the stones where the smallest.

From all synthetic crystals in powder form, a small amount of the powder was placed on the microscope slide and spread out as much as possible before covering them with a cover glass. Crystals where measured in areas where the crystals where separated from each other as much as possible and the measured objects where approximately 10 μm long. The corticosteroids where treated in the same way as SF.

2.2 Equipment set-up

The Raman spectrometer that was used in this research was a home-built Raman spectrometer integrated with the base of an Olympus BX41 upright microscope. To see if polarization microscopy and Raman spectroscopy can be combined, it was essential for the goal of this study to add polarization filters to the available Raman spectrometer to create a polarizing effect. The next sections describe the integration of polarization microscopy and how the system was used.

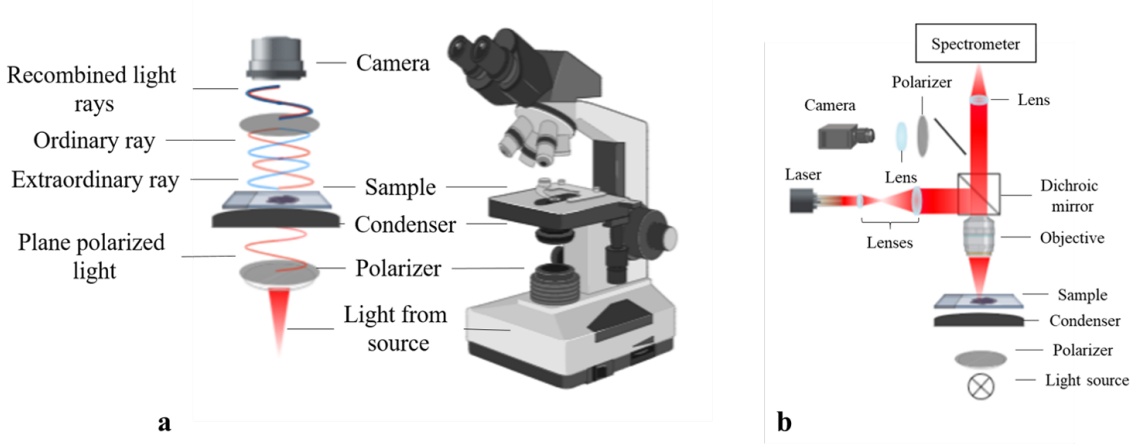

Figure 4: Representation of microscope set-up. a) Optical pathway after polarization filters. b) pathway of Raman laser.

2.2.1 Integration of polarizing filters

The microscope (Olympus BX41) used in the Raman set-up, was modified for in-house polarization microscopy. Two linear polarization filters were placed in the light path. The polarizer was placed between the light source and the object plane, before the condenser, to convert unpolarized light into linearly polarized light. The polarization analyser was placed between the objective and the CCD camera lens. Initially, a 30 Watt halogen light was used but because this produced too much heat it had to be replaced. An ultra bright LED light was used but the emitted power was too low. Therefore a better LED was found and the final light was a single-colour Surface-Mounted-Device (SMD)-LED (Farnell, LXML-PD01-0040) with an optical emitted power pf 46 mW at 627 nm with a bandwidth of 20 nm. This resulted in an image of 1024x768 pixels and an optical resolution of 677 nm. This was enough to measure a high signal from the

crystals when the polarization filters were at perpendicular angles to each other. The signal intensity was strongly dependent on the type of crystal and on their orientation. Appendix A shows the grey scales of crystals with strong and weak birefringence and the resulting Raman spectra. The figure shows that weaker birefringent objects could be easily recognised and surrounding birefringent objects as well. Additionally, the figure shows that a strong birefringence did not necessarily translate to a higher Raman signal.

2.2.2 Raman microscope

Microscope images were taken in transmission mode with a 40x 0.95NA super apochromat objective (Olympus). The CCD camera had a chip for 1024x768 pixels with a total field of view of 108 µm x 81.6 µm and an optical resolution of 330 nm, which made the crystals, that are typically in the range of 10 µm, easily visible. The samples were brought into focus by manually adjusting the z-axis of the microscopic stage. Then, the polarizer at the base of the microscope, was oriented in such a way that the polarizing filters were at a 90° angle to each other to achieve a dark spot. When the dark spot is achieved, only birefringent specimens will transmit light through both polarizers over the whole field of view. A krypton ion laser operating at 647.09 nm (Innova 70C ion laser, Coherent) was focused on the sample to produce Raman scattering. The Raman scattered light was collected through the same 40x/0.95NA super apochromat objective and dispersed in a spectrometer and collected with a CCD sensor (Andor Newton DU-970-BV). The Raman signal was obtained from 0-3600 cm^{-1} through a raster scan on a 40x40 pixel grid with and the optimal Raman signal was obtained with an illumination time of 250 ms per pixel and a chosen region of interest (ROI) frame of 10x10 μm which brought the total measurement time to just under 7 minutes. The step size was small because a crystal such as MSU can be as thin as 1 μm in width and if the stepsize is too big, the signal cannot be measured.

2.2.3 Calibration

On each day that samples were measured, the intensity and wavelength of the Rayleigh-Raman spectrometer was calibrated to convert the raw data to calibrated data in wavenumber (cm^{-1}) vs counts. The pixel-to-wavenumber conversion was performed by measuring the Raman spectrum of liquid toluene and using an argon-mercury lamp. The Raman peaks in the toluene spectrum are known relative wavenumber shifts with respect to the exciting laser line at 0 cm^{-1} shift. The argon-mercury lamp has narrow emission lines with an accuracy up to picometer precision. An intensity calibration was performed to correct the wavelength-dependent transmission of the Raman setup and the pixel-to-pixel variation in the detection sensitivity of the CCD camera. This was done by acquiring a white light spectrum from a tungsten halogen light source (AvaLight-HAL; Avantes BV, Apeldoorn, the Netherlands). The offset of the detector was obtained with a measurement where no light was falling onto the detector. Lastly, a background measurement where the spectrum of the entire light path through the setup with the laser on was obtained and later subtracted from all measurements.

2.3 Data analysis

To create a platform that can be used to identify different crystals in SF, the data analysis was divided into three parts: 1) development of a data analysis model to generate a Raman spectrum that can be placed in the database or be stored as a measurement, 2) building a database and 3) applying the database. In the database, all expected crystals spectra as previously mentioned were placed. To identify a newly measured crystal, the Raman spectrum would be correlated with all Raman spectra in the database. All data processing and analysis was performed in Matlab 2019b (Mathworks, Eindhoven, the Netherlands). The pathway of all data processing steps can be found in figure 6 which will be explained in detail in the next sections.

2.3.1 Development of a data analysis model

All raw data of the measurements from one day were processed with the calibration data from the same day as described in the previous section. This would result in files that could be used in Matlab for further data processing (mQCR files). One measurement, and therefore one mQCR file, contained 1600 Raman spectra from each measured pixel. The mQCR files were loaded one by one in the next program to obtain the crystal data. In the pre-treatment steps the spectral interval between 300 and 1800 cm^{-1} was selected in the data. Then cosmic rays and outliers were removed. These were detected by calculating the median from the data and comparing this to six times the standard deviation of the data as can be seen in formula 1. Here, y represents the data, Med is the median and σ is the standard deviation. The median and standard deviation are based on the 1600 Raman spectra. Any peaks that exceeded this threshold were replaced by an interpolated spectrum. Then, all data was interpolated to the same grid of 750 data points from 300-1800 cm^{-1}.

$$|y - Med(Y))| > 6\sigma(Y)) \tag{1}$$

The data then underwent baseline correction using the Whittaker baseline subtraction over the interval of 300-1800 cm^{-1}. This function fits different lines to the data-sets and calculates the distance between the fitted line and the actual data and squares them. The best lines is considered to be the one with the lower sum of squares. To avoid over-fitting the data and thus removing important peaks in the Raman spectrum, the function checks for variation in the data-points. If there is suddenly a big shift between two data-points, which happens in case of a peak, a penalty is added to the sum to increase the value of the fitted line. After baseline subtraction, the data was normalised with z-score normalisation which uses formula 2.

$$z = \frac{x - \overline{X}}{S} \tag{2}$$

This formula describes the z-score of a data point x from sample data with mean $\overline{X}$ and standard deviation S. The z-score is returned such that each Raman spectrum from the 1600 are centered to have mean 0 and to have standard deviation 1. Finally,

multivariate analysis of the Raman spectra was performed with principal component analysis (PCA). PCA was performed on the spectral region between 300 and 1800 cm^{-1}. PCA uses multidimensional scaling to linearly transform variables to a lower dimensional space but still preserving as much of the data's variation as possible. The most relevant information from the spectral data matrix is extracted with PCA. It is then shown as a linear combination of orthogonal principal components with loadings (scores) for the contribution of the variance to the data. A single score value was assigned to each measured pixel in the ROI and a Raman image was reconstructed based on the scores. A high score of a certain loading indicated a high contribution of that loading to that specific pixel, which can be representative for a substance. The first principal component can be defined as the direction with maximum variance of the projected data. Here, the first nine principal components were used which should have captured most of the variance in the data. All Raman spectra used in this study where created by using the results from the PCA scores plots. This will be further explained in the following sections.

2.3.2 Building a database

Ideally, the database should contain Raman spectra of all components that were expected to be present in SF. Because not all components were directly found in SF, synthetic components were used in addition to the findings in patient samples. Additionally, the Raman spectra in the database had to have as little contribution from SF components as possible. Figure 5 shows how a crystal Raman spectrum was created. Out of nine scores plot that resulted from the PCA, the plot that represented the crystal most was manually selected. Each scores plot contained 1600 pixels where each pixel contained one Raman spectrum. From the chosen scores plot, the minimum pixel value that represented the crystal was selected and all pixels above this value were averaged to create one Raman spectrum representing the crystal. Then, the maximum contribution to the background was selected and all pixel values lower than this value were averaged and subtracted from the crystal spectrum.

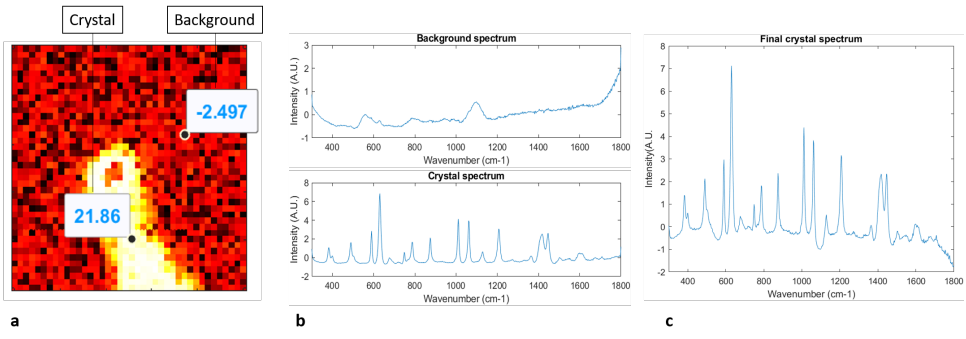

Figure 5: Data processing where in a) the scores plot representing a crystal from yellow to white pixels corresponding to high score values compared to the background represented with the red to black pixels which results in b) an average crystal spectrum and a background spectrum that is subtracted which leads to c) a Raman spectrum that is placed in the database or saved as a measurement

2.3.3 Using the database

In each sample, five birefringent objects were measured on average and processed as single spectra. The amount of crystals in an SF sample varied between 1-2 crystals per field of view up to 10-20 crystals per field of view. Once all measurements were performed, each single spectrum that was collected from the crystals was correlated with the Raman spectra in the database with the corrcoef Matlab function. Matlab uses the Pearson correlation coefficient which is defined as in Equation 3 where the correlation coefficient of two random variables with N scalar observations is defined as:

$$\rho\left(A,B\right)=\frac{1}{N-1}\sum_{i=1}^{N}\left(\frac{\overline{A_i-\mu_A}}{\sigma_A}\right)\left(\frac{B_i-\mu_B}{\sigma_B}\right) \tag{3}$$

with μ and σ as the mean and standard deviation of variables A (database component) and B (Raman spectrum from measurement) respectively. This function resulted in the calculation of the Pearson correlation coefficient which is a number between minus one, zero and one. Zero represents no correlation, one represents a perfect positive and minus one a perfect negative correlation. The correlation strength of the association between one measurement and all database components was determined. Finally, the measured crystals were identified by using the database components with the highest correlation with each single crystal spectrum. In the end an overview was created with the expected component(s) (according to the diagnosis from a Rheumatologist), the found component according to the database and the strength of the correlation between the measurement and the database component. This way it was possible to compare the initial diagnosis to the measured components and to possibly confirm the initial diagnosis, to identify components that were not recognised by Rheumatologists and to specify those components on the basis of the information in the database.

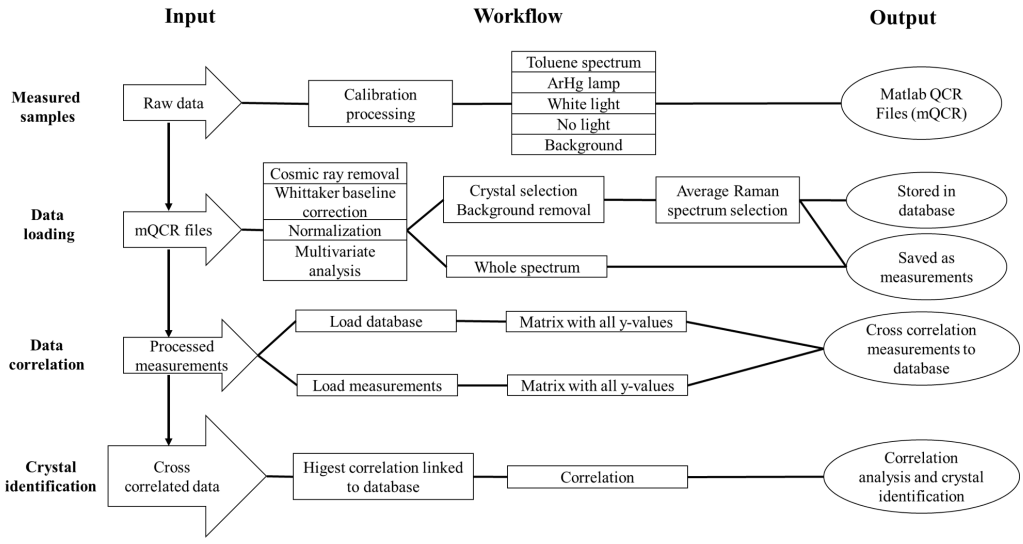

Figure 6: Schematic representation of data processing from when the measurements were performed

3 Results

In this section, different results of the study are presented from equipment optimization to data analysis.

3.1 Optimization polarization integration

Different approaches were used to optimize the intensity of the signal after placing the polarization filters in the optical pathways. The final set-up that allowed the most light to pass through the system was achieved with a single-chip SMD LED with a power of 2 Watt and when the condenser was placed exactly underneath the sample. This way it was possible to also image weakly birefringent specimens in the sample. The bright field image and polarized image can be found in figure 7. The camera provides 8-bit images.

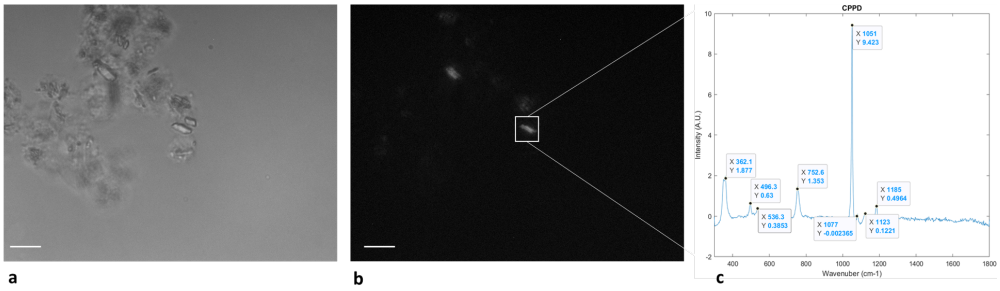

Figure 7: Example of the integration of the polarization filters with a) original brightfield image of an SF sample where crystals are seen surrounded by cells b) image when polarization filters are turned in such a way that a dark spot is achieved and c) resulting Raman spectrum from a detected crystal in polarization mode (CPPD crystal) after data processing. Scale bar = 10 µm

3.2 Building a database

The database was constructed and optimised during the study. In the first database (N1 in the table), it was assumed that CPPD was one type of crystal. With this assumption in the database, an overview was made to see how the data was divided (table 3). The overview shows how many times different correlation strengths were found between the measured Raman spectra and the database. This database contained 13 Raman spectra of crystals.

The database was improved by dividing CPPD in three categories: triclinic CPPD (t-CPPD), monoclinic CPPD (m-CPPD) and dimorphic CPP tetrahydrate (m-CPPT β). Additionally, the Raman spectrum of calcium carbonate was found in the form of calcite. All components were added to the second database which then contained 17 Raman spectra. By adding these components, the components that correlated poorly ($r < 0.6$) were reduced by almost half from 97 to 59. The third improvement, N3, of the database was the definition of calcium carbonate in aragonite form. Calcite and aragonite have the same chemical formula $CaCO_3$ but their atoms are stacked in

different configurations which cause slight shifts in the Raman spectrum. Defining this sub-species resulted in an improvement in the high correlations (r > 0.9) from 39 to 47 compared to the second database N2. The final database contains 18 Raman spectra. All Raman spectra that were placed in the database can be found in appendix B.

Table 3: Overview of the number of measured Raman spectra that correlated with Raman spectra from the database in different correlation strengths. N1 is the number of correlations resulting from the first database. N2 and N3 are results from improvements made to the database.

Correlation coefficient	N1	N2	N3
r $\geq$ 0.9	26	39	47
0.8 $\leq$ r <0.9	38	57	54
0.7 $\leq$ r <0.8	16	23	18
0.6 $\leq$ r <0.7	21	19	20
r $\leq$ 0.6	97	59	56

3.3 Crystal detection using data correlation

With the improved database, 195 measurements were used for data analysis. Three measurements where not used. With the information obtained from the correlation between the single Raman spectra and the database components, several findings were made that will be discussed in the following sections. The correlation strengths that were analysed ranged from lower than 0.6 to a correlation higher than 0.9. The correlation strengths were classified as follows:

r $\geq$ 0.9	Excellent
0.8 $\leq$ r <0.9	Very good
0.7 $\leq$ r <0.8	Good
0.6 $\leq$ r <0.7	Fair
$\leq$ 0.6	Poor

3.3.1 MSU detection

Out of 195 measurements, 54 Raman spectra were predicted to be MSU, based on the judgement of the researcher. It was calculated how many times MSU was predicted and also how many times it was observed with different correlation strengths. As can be seen in figure 8, eleven measurements that were predicted to be MSU correlated with an excellent correlation strength. 25 MSU values correlated very good with MSU from the database. Six Raman spectra that were predicted to be MSU correlated with another spectrum from the database which can be found in appendix C figure 16. One of these Raman spectra correlated fair and five Raman spectra correlated poorly.

From these measurements, five correlated with the cholesterol Raman spectrum and one correlated with t-CPPD. Looking at the Raman spectra that correlated fair or poorly, it can be seen that all Raman spectra are either missing characterising Raman peaks, such as the main peak at 631 cm^{-1}, or have some additional peaks that are not consistent with the MSU Raman spectrum.

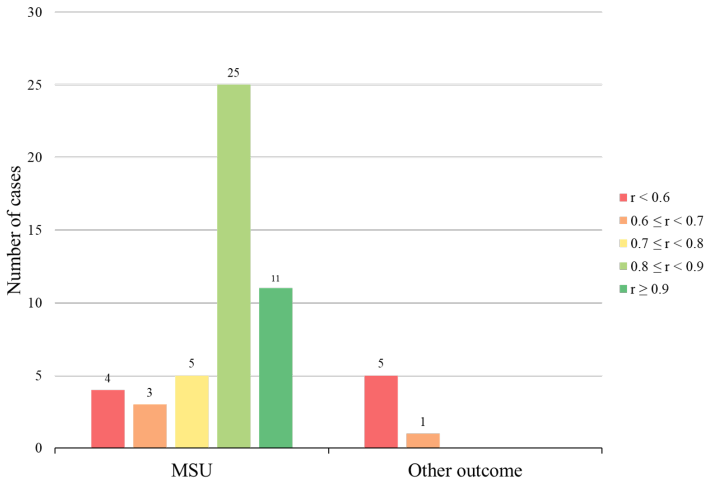

Figure 8: Number of times MSU was predicted and the measured Raman spectrum correlated with MSU or another component from the database with different correlation strengths.

The Raman spectra that were predicted to be MSU and correlated with MSU but with an fair correlation (Appendix C, figure 17), show that all except one of these Raman spectra has at least the characteristic peak around 630 cm^{-1}. In these spectra it can be seen that this peak is either not the main peak, that part of the MSU spectrum is missing or that too much background was subtracted from the Raman spectrum leading to negative peaks in the Raman spectrum.

3.3.2 CPPD detection

48 measured objects were predicted to be CPPD based on their Raman spectrum. 39 Raman spectra were divided within the sub-categories of CPPD by the correlation as can be seen in figure 9. 24 Raman spectra correlated with a database component with an excellent correlation. Sixteen were classified as t-CPPD, three as d-CPPt β and five as another component. 20 Raman spectra correlated with very good, of which twelve correlated with t-CPPD, four with m-CPPD, one with d-CPPt β and one as another component. From the components that were classified as other, two correlated poorly (see appendix D). One of these spectra correlated with cholesterol (r=0.11), the other correlated with hydroxyapatite (r=0.27). When looking at the Raman spectra, it can be seen that neither of these spectra represent any of the characteristic peaks for the CPPD sub-types. The remaining nine Raman spectra that were classified as other were identified to be different forms of calcium carbonate and will be discussed in section 3.3.4.

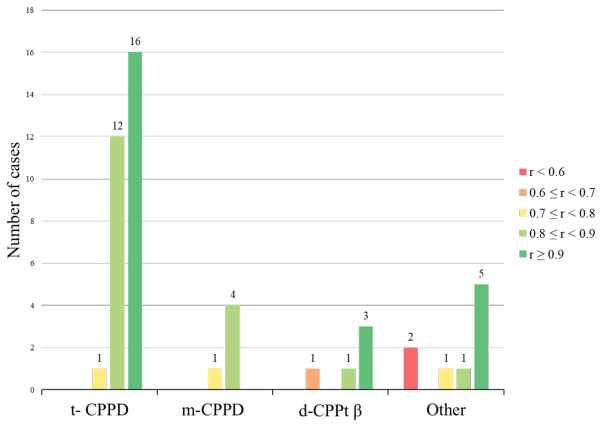

Figure 9: Number of times CPPD was predicted and the measured Raman spectrum correlated with a CPPD sub-category or another component from the database with different correlation strengths.

3.3.3 Detection of unknown components

From all measurements, 75 Raman spectra were classified as unknown. Figure 10 shows how these Raman spectra were correlated with all components in the database with different correlation strengths. The figure shows that seven components were identified with an excellent correlation strength. These components are t-CPPD (1), calcite (1), aragonite (2) and KenaCort (3). Eight components where identified with a very good correlation strength. These are MSU (2), m-CPPD (2) and aragonite (4).

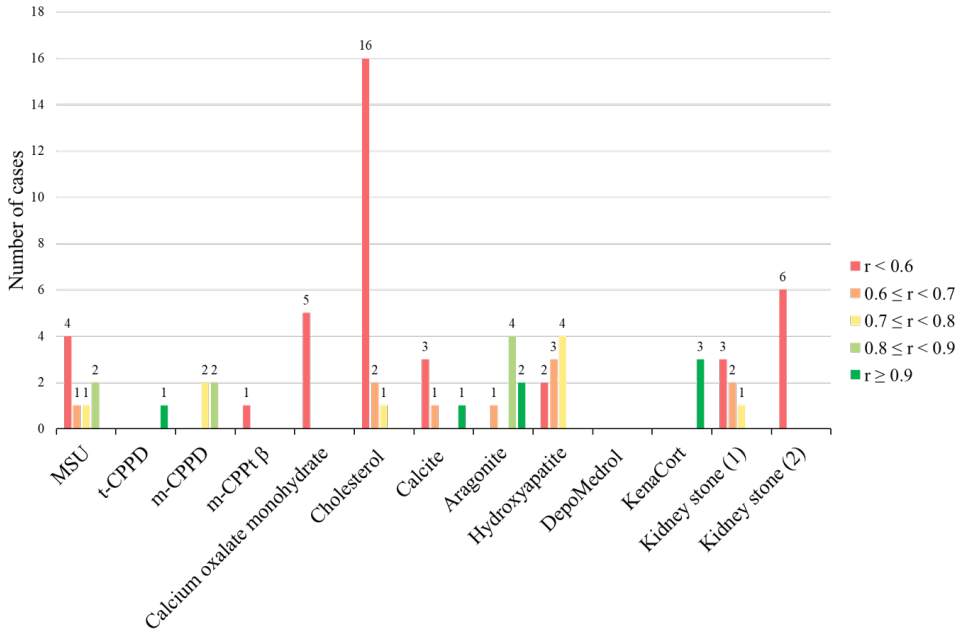

Figure 10: Number of times the Raman spectrum was unknown and correlated with components from the database with different correlation strengths.

Notable in this graph is that 43 Raman spectra correlated poorly with the database and that a great portion of these are correlated with cholesterol. Looking at some of these Raman spectra (appendix E) it can be seen that most of the spectra do not have the characteristic peak for cholesterol at 700 cm^{-1} but that the spectra do have broad Raman peaks around 1440 cm^{-1} and 1660 cm^{-1} which are similar to the Raman spectrum of cholesterol.

3.3.4 Detection of new crystals

During the study, many unknown Raman spectra were measured. Calcium carbonate crystals were found in the form of calcite and aragonite. Adding these Raman spectra to the database revealed the substances to be present in more patient samples (see figure11). Eleven Raman spectra correlated with calcite of which six with an excellent correlation, one with a good correlation, one with a fair correlation an three with a poor correlation. Four Raman spectra correlated excellent with aragonite, five correlated very good and one correlated fairly.

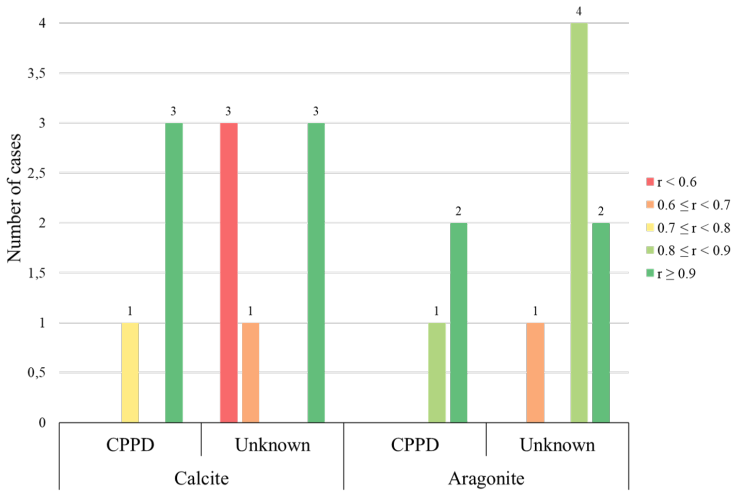

Figure 11: Number of times calcium carbonate crystals in the form of calcite and aragonite were found with different correlation strengths when the Raman spectrum was predicted to be CPPD or the Raman spectrum was unknown

The poor correlating Raman spectra can be found in Appendix F. have similar peaks to the calcite spectrum in the database but are slightly shifted. Additionally it can be seen that these Raman spectra contain additional peaks that do not represent the calcite spectrum. Other unknown Raman spectra have currently not been identified.

3.3.5 Synthetic crystals

Lastly, all synthetic components that were measured were correlated with the database to see how much this data associated with their respective components from the database. Figure 12 shows that all but two Raman spectra correlated with their respective database components and that eight measurements correlated with an excellent correlation, three measurements correlated with a very good and another three with a fair correlation.

The poorly correlating Raman spectrum and the measurements that did not correlated with their respective database components can be found in Appendix G. The poorly correlating MSU Raman spectrum does contain all characteristic peaks but the signal is really low. One synthetic cholesterol sample did not correlate with cholesterol but with the substance found in one of the kidney stones (r=0.26). This spectrum did contain the peak that is characteristic for cholesterol at 696 cm^{-1}, the rest of the Raman spectrum however, contains a lot of noise. One Raman spectrum that was supposed to be calcium oxalate monohydrate but correlated with MSU. This Raman spectrum is more similar to calcite with peaks at 712 and 1065 cm^{-1} Additionally,

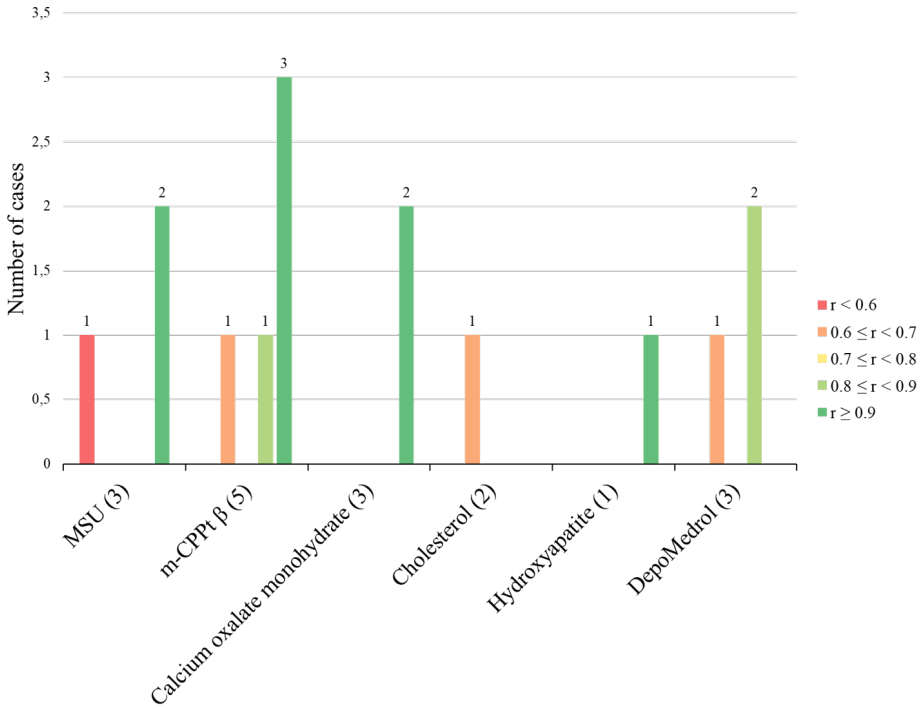

Figure 12: Number of times the Raman spectra from synthetic crystals correlated with their respective database components with different correlation strengths. The numbers indicate the amount of times the components were measured.

3.4 Patient diagnosis

After evaluating the effect of correlating measurements to a database, it was assessed how this would translate to the individual patient samples. All diagnoses from the Rheumatologists were compared to the findings from the Raman measurements. This was done by using correlation-based crystal identification and these results can be found in table 4. This table contains the compounds that correlated with the database with at least, what was considered, a good correlation. From the 22 patient samples, six samples were indicated to contain only MSU, two samples where indicated to contain only CPPD, one sample indicated a combination of MSU, CPPD and Kenacort, two samples where kidney stones, one sample contained maltese cross like crystals, another sample contained no crystals and from nine samples the indication from the Rheumatologist was not provided. Thirteen samples were provided with an indication from the Rheumatologists. In five of these cases, the found components matched with the provided indication. This includes the two kidney stones where COM was measured which is a major component of kidney stones. In sample four, the indicated component was found with an additional component. In sample nine, the indication partly matched the found components but an additional compound was found. In samples six, seven and eight, the indication from the Rheumatologist did not match with the found components. In samples fourteen, fifteen, sixteen, nineteen and twenty where the content was unknown, one component was identified. In sample 18 and 22, two components where identified, in sample 21, two components where identified and one unknown component was found. In sample 17 only a component was found but the Raman spectrum was not clear enough to make out the substance. In this table, only the measurements that correlated higher than 0.7 are included. The full table with all correlations can be found in appendix H. If more than one substance is mentioned, this means that both the substances where found in separate measurements.

Table 4: Comparison between object identification in SF by Rheumathologist and found components with the combination of CPLM and Raman spectroscopy.

Sample number	**Diagnosis from Rheumatologist**	**Found with Raman**
1	MSU	MSU
2	MSU	Unknown Raman spectrum
3	MSU	MSU
4	MSU	MSU, Calcite
5	MSU	Two unknown Raman spectra
6	MSU	Hydroxyapatite, Aragonite
7	CPPD	Calcite
8	CPPD	Aragonite
9	MSU, CPPD, KenaCort	Calcium oxalate monohydrate, t-CPPD
10	Kidney stone	Calcium oxalate monohydrate
11	Kidney stone	Calcium oxalate monohydrate
12	Maltese cross	Two unknown Raman spectra
13	No crystals	No crystals
14	Unknown	t-CPPD
15	Unknown	MSU
16	Unknown	MSU
17	Unknown	Unclear Raman spectra
18	Unknown	Aragonite, t-CPPD
19	Unknown	Calcite
20	Unknown	MSU
21	Unknown	m-CPPD, t-CPPD, Unknown Raman spectrum
22	Unknown	t-CPPD, Kenacort

4 Discussion

The goal of this study was to combine Raman spectroscopy with polarization microscopy to improve the diagnosis of crystals in synovial fluid. The current diagnostic problem is that not all crystals are correctly identified with just CPLM. This is because of similarities between crystals that are sometimes overseen even by specialised personnel. Another goal of this study was to construct a platform that would make it possible to identify crystals measured with Raman spectroscopy by correlating the Raman spectra with a database that was constructed of Raman spectra from crystals that are known to be present in SF. To achieve this goal, different sub-questions were also constructed and this section will discuss all questions in relation to the results. By integrating polarization filters into the Raman set-up and developing a data analysis platform, it was possible to detect multiple components that are not distinguishable in the current clinical setting. Different components were found that have not or only scarcely been mentioned before such as calcium carbonate derivates calcite and aragonite. Additionally, different forms of CPPD were defined and distinguishable with the developed correlation algorithm.

First, Raman spectroscopy was combined with polarization microscopy was performed by integrating polarization filters into a home-built Raman set-up. Different optimisation steps were needed to detect the highest signal from the crystals such as increasing the power of the light source and adjusting the placement of the condenser. There are still limiting parameters that require optimisation. For instance, the CCD camera provides only 8-bit images. When the field of view would contain both a weak and strong birefringent specimen, it is possible that the weak birefringent specimen is not visible anymore. Additionally, the images are in grey-scale which makes it impossible to distinguish positive from negative birefringence. However, much newer equipment is used in clinical settings which would mean that the limits from this study are not necessarily limiting for introducing Raman spectroscopy to the clinic. Overall, once the light source was powerful enough and the condenser was positioned correctly, most crystals, which were approximately 10 μm on average, could be observed. The intensity of the signal from the crystals varied, and was partly dependent on the orientation of the crystal. As shown in Appendix A, the intensity of the Raman signal was not necessarily dependent on the intensity of the signal from the crystals. There are other factors that do affect the Raman signal. The orientation of the crystal can affect the Raman signal and cause small shifts in the Raman spectrum [58]. Another factor that can influence the Raman measurement is the presence of cells in SF which is part of the immune response. While these intra-cellular crystals are visible with polarization microscopy, measuring these crystals with Raman spectroscopy can cause interference. The presence of cells can mostly be filtered out by PCA but it is possible that small contributions of the cells to the Raman spectrum of the crystal still occur.

The current measurement time is close to seven minutes. In a clinical setting, where more than one crystal needs to be measured per patient, this is not ideal. During this study, 1600 pixels were measured with an illumination time of 250 ms per pixel. To reduce the measurement time, a smaller frame could be used or just a part of a frame

where a line could be drawn through the object. In some cases, the crystals could not be measured immediately because the content of the SF was floating through the sample. In this case, the sample would be left to dry for approximately thirty minutes which also is not optimal in a clinical setting. A smaller sample volume might be a solution because the sample might spread faster over the microscope slide. This could however, also lead to that not all components will be observed because of lower sample volume. Another solution might be the use of different microscope slides with channels but here the cost of of the material should also be taken into consideration. Additionally, a method to enzymatically digest SF could be used to collect all crystals as previously mentioned [52]. This way, all organic debris can be filtered and only the crystals would remain. The study that describes this method mentions that with this method the MSU and CPPD crystals are not degraded. This should be confirmed for other crystals. Additionally the process of this enzymatic digestion takes more than hour and should therefore also be optimised if this would be a promising method.

After optimising all optical settings, the data processing was optimised. During the selection of the spectral data of the crystal during PCA analysis, a contribution of background signal is also selected and subtracted from the crystal spectrum. In some measurements this may have led to over-subtraction leading to negative peaks in the final Raman spectra. To prevent over-subtraction, a fitting function that first fits the background spectrum to the crystal spectrum before subtraction could be used instead of just subtracting the background spectrum. Another method to select only the crystal spectrum would be by hierarchical cluster analysis. This method uses the information from the PCA to create clusters of the available data. This way, a cluster representing the crystal could be selected and the average Raman spectrum could be extracted. In some Raman spectra it can also be seen that at the beginning and the end of the spectra a large peak upwards or downwards is observed (see appendix F, figure 20a and b). This was probably caused by the Whittaker baseline subtraction function. This function was used on only the interval 300-1800 cm^{-1} rather than over the whole Raman spectrum. When taking the entire Raman spectrum and these peaks would be observed at the beginning and the end, they would not contribute to the Raman spectrum anymore when the interval 300-1800 cm^{-1} was selected. It is important to evaluate the way the data was processed because every step influences the Raman spectra and can influence the correlation of the data with the database.

An important factor in constructing a database is understanding the components that go into the database. This became clear when CPPD was divided into sub-categories and calcite and aragonite were identified which improved the outcome of the correlations. This change has led to the observation that most correlated Raman spectra could be correlated with a correlation coefficient higher than 0.8 and it is expected that further optimisation of the database can further improve the numbers. Characterising more unknown Raman spectra would be one way to further optimise the database. A number of Raman spectra were found that could not be identified with the available knowledge on crystals in SF. Another way to improve the database is to expand it with more of the same Raman spectra but with little shifts in the spectra. This way when a new measurement is run through the database it has a

higher chance to be detected even when the spectrum is slightly shifted from the expected Raman spectrum. Additionally it could be helpful to detect characteristic peaks in the Raman spectra after the correlation is performed. In some measurements, the correlation was correct, meaning that the correct database component correlated to the measurement, but the correlation coefficient was lower than 0.6 (see appendix C figure 17). An additional check for characteristic Raman peaks could help in the cases that the correlation is not straightforward. A previous study [59] already developed a model to identify Raman spectra by using this exact function. However this model was quite complicated and not fully optimised. By using part of this program to only identify the main peak (in the case of MSU around 630 cm^{-1}) to aide the correlation program and maybe reduce data processing time.

By using the database, 87 measurements that were predicted to be MSU or a form a CPPD, were correctly identified with varying correlations. An interesting find was that a large portion of the unknown Raman spectra correlated poorly with cholesterol. Cholesterol is a substance that has many Raman peaks which might be the reason why it correlates with many spectra that are probably not cholesterol. One synthetic cholesterol Raman spectra correlated fair with the cholesterol Raman spectrum in the database which was also synthetic. Another synthetic cholesterol measurement did not even correlate with the database cholesterol. These Raman spectra were expected to be nearly identical since it was the same substance and there was no background interference from SF. Therefore, the Raman spectrum of cholesterol is thought to cause a lot of interference with other components as seen in MSU detection (see figure 8). These observations should be assessed carefully to prevent that wrong conclusions are drawn from these observations.

The Raman spectra of calcium carbonate in the form of calcite and aragonite were initially not expected to be found. With polarization microscopy, these components were not distinguishable from CPPD crystals as they have similar shape and are also negatively birefringent. Upon measuring, the Raman spectrum was unknown and often classified as CPPD. Literature searches revealed that the Raman spectrum represented calcite based on the similar peaks found around 1086 and 712 cm^{-1} and peaks at 1085 and 706 cm^{-1} for aragonite [60] [61]. Calcite and aragonite are anhydrous crystal form of calcium carbonate. Depending on the conditions, the polymorphisms can transform between each other. The type of polymorphism that will form depends on environmental factors such as pH and temperature [62]. Calcite and aragonite are known components in gall stones [63], but literature is lacking on these crystals in SF. One study that focused on the evolution of calcium phosphate precipitation *in situ* measured with Raman micro-spectroscopy, found that calcite formation is strongly dependent on changes in the pH [64]. Calcite and aragonite were found in multiple patient samples (see table 4 in section 3.4) and therefore it is interesting to further analyse where this compound originates from.

Another find in the patient samples was hydroxyapatite (see table 4 in section 3.4). This crystal is not birefringent and also very small (75-250 nm). Therefore, detecting it with Raman spectroscopy in polarization mode is quite surprising. The correlations were not in the highest segment but with an r of 0.78 and 0.75 and further

inspection of these Raman spectra it was confirmed that they were the Raman spectra of hydroxyapatite. The confirmation was based on the peaks at 426, 588, 958, 1044 in the Raman spectrum placed in the database (see appendix B, figure 15e,f) and similar peaks described in literature [65]. With the database it was also possible to identify the corticosteroid Kenacort in SF. Rheumatologists from VieCuri have indicated that finding this compound is difficult with only CPLM because of similarities with other crystals. With the addition of Raman spectroscopy it is easily distinguished from other crystals.

Overall, the differences observed between the indication from the Rheumatologists and the measured components with Raman spectroscopy are interesting. In some patient samples the indicated components were not even found. This does not mean that the component was not there but it was not detected. It does mean that there is much more information to be gathered from SF than the currently available information. It should be assessed how many crystals in a sample need to be measured to create an accurate picture of all components in SF. Additionally, a method should be found to obtain and centralise all crystals present in a patient sample. In this study, approximately five measurements per sample were performed which is probably too little to create the full picture. When the full picture is there, hopefully more accurate diagnoses and possibly underlying pathologies and metabolic changes come to the surface which could greatly improve treatment options and patient care. Additionally, it could be valuable to measure SF from healthy donors but this is difficult to obtain because in healthy conditions. SF is only present in very small amounts.

In conclusion, it was shown that combining Raman spectroscopy with polarization microscopy can provide much new, valuable information. It was also shown that crystal detection is possible by correlating new Raman measurements with a database of known components. By using this platform it was possible to categorise CPPD crystals and even a new component was found namely calcite. Additionally it was possible to identify the corticosteroid Kenacort in one of the patient samples by using the database. Optimisation for different aspects such as data processing and SF sample preparation are still required but this study has provided a foundation to work toward an improved diagnosis of crystals in SF by combining Raman spectroscopy with polarized light microscopy.

5 Future perspectives

Many steps still need to be taken to bring Raman spectroscopy to the clinic. Different optimisation steps were already discussed in the previous section. This section will describe additional means that are thought to be necessary to optimally combine Raman spectroscopy with polarization microscopy.

Currently, SF samples are obtained from the patients and viewed under a microscope directly after aspiration. If Raman spectroscopy would be implemented, an automated program that detects birefringent objects could be developed. In Appendix A it is already shown that by viewing crystals in polarisation mode, the birefringent objects can be distinguished from the rest of the components in the sample. Ideally, an automated program would detect birefringent objects, determine an area that should be measured and instantly obtain the Raman spectrum from the object. The obtained data is then also immediately processed and correlated to obtain a diagnosis. Instead of measuring an 10x10 μm area with 1600 pixels, an area based on the detection of the birefringent object could be automatically determined to increase the speed of the measurements. This concept is illustrated in figure 13. Several birefringent objects would be measured and in each object, an area on the object is selected in the form of the line and the Raman spectrum is obtained from one object. This spectrum is run through the database and a correlation is provided with a corresponding subject. This is repeated for all birefringent objects in one field of view and eventually a diagnosis is provided with all components found in the sample.

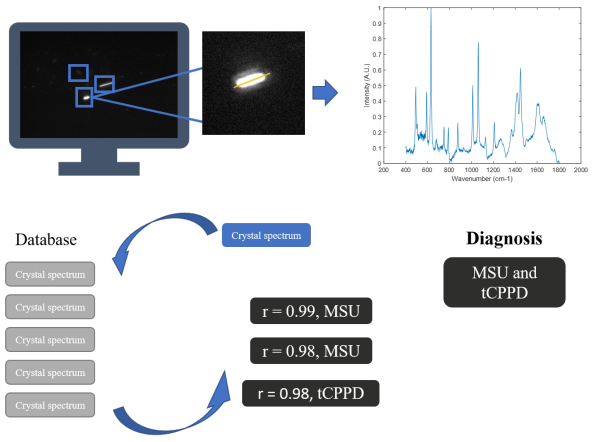

Figure 13: Future automated program to detect crystals in SF: birefringent objects are detected by an automated program which selects an area in the form of a line to be measured per object. This results in a Raman spectrum per measured object that is automatically run through the database. The database then outputs the correlations with the indications and provides a diagnosis.

Ideally, the sample would be pre-treated in such a way that all crystals are isolated and centred in one place so that all crystals are visible simultaneously. Many steps still need to be taken to get to the point that Raman spectroscopy can be integrated and used in the clinic but this study provides the first steps and a foundation to further develop this concept.

Bibliography

[1] Michele M. Temple-Wong et al. "Hyaluronan concentration and size distribution in human knee synovial fluid: Variations with age and cartilage degeneration". In: *Arthritis Research and Therapy* 18.1 (2016), pp. 1–8. ISSN: 14786362. DOI: 10.1186/s13075-016-0922-4. URL: http://dx.doi.org/10.1186/s13075-016-0922-4.

[2] Osteoarthritis A Karen Esmonde-White et al. "Raman Spectroscopy of Synovial Fluid as a Tool for Diagnosing". In: *J Biomed Opt* 14.3 (2009). DOI: 10.1117/1.3130338.

[3] Tamer Mahmoud Tamer. "Hyaluronan and synovial joint: Function, distribution and healing". In: *Interdisciplinary Toxicology* 6.3 (2013), pp. 111–125. ISSN: 13376853. DOI: 10.2478/intox-2013-0019.

[4] R Sloot et al. *Reumatische aandoeningen in Nederland: ervaringen en kengetallen.* Tech. rep. NIVEL, 2016. URL: http://www.nivel.nl.

[5] Monica Zell, Dawen Zhang, and John Fitzgerald. *Diagnostic advances in synovial fluid analysis and radiographic identification for crystalline arthritis*. Mar. 2019. DOI: 10.1097/BOR.0000000000000582.

[6] M.D Harris, L.B Siegel, and J.A Alloway. "Gout and Hyperuricemia - American Family Physician". In: *Am Fam Physiscian* 59.4 (Feb. 1999), pp. 925–934. URL: https://www.aafp.org/afp/1999/0215/p925.html.

[7] Fernando Perez-Ruiz and Nicola Dalbeth. *Gout*. Nov. 2019. DOI: 10.1016/j.rdc.2019.08.001.

[8] Kenneth L Rock, Hiroshi Kataoka, and Jiann-Jyh Lai. "Uric acid as a danger signal in gout and its comorbidities". In: *Nat Rev Rheumatol* 9.1 (2013), pp. 13–23. DOI: 10.1038/nrrheum.2012.143.

[9] Miguel A Martillo, Lama Nazzal, and Daria B Crittenden. "The Crystallization of Monosodium Urate". In: *2Curr Rheumatol Rep* 16.2 (2014). DOI: 10.1007/s11926-013-0400-9.

[10] Fasih A. Hameed. "Gout". In: *Integrative Medicine: Fourth Edition*. Elsevier, Jan. 2018. Chap. 69, 689–696.e2. ISBN: 9780323496179. DOI: 10.1016/B978-0-323-35868-2.00069-4.

[11] Ashika Chhana, Gerald Lee, and Nicola Dalbeth. "Factors influencing the crystallization of monosodium urate: a systematic literature review". In: *BMC Musculoskeletal Disorders* (2015). DOI: 10.1186/s12891-015-0762-4.

[12] Martin Underwood. *Clinical review Diagnosis and management of gout*. Tech. rep. 2006.

[13] *Pseudojicht (CPPD)*. URL: https://reumatologie.slingeland.nl/kenniscentrum/Ziekte-aandoening/Kristalartritis/Pseudojicht-%7B%5C%%7D28CPPD%7B%5C%%7D29/2590/2602/2717 (visited on 09/28/2020).

[14] Shira G. Ziegler, William A. Gahl, and Carlos R. Ferreira. "Disorders and Mechanisms of Ectopic Calcification". In: *Genetics of Bone Biology and Skeletal Disease: Second Edition*. Elsevier Inc., Jan. 2018, pp. 571–595. ISBN: 9780128041987. DOI: 10.1016/B978-0-12-804182-6.00032-0.

[15] A.K Rosenthal, N Dalbeth, and P.L. Romain. *Clinical manifestations and diagnosis of calcium pyrophosphate crystal deposition (CPPD) disease - UpToDate*. June 2018. (Visited on 05/18/2020).

[16] Pranav Oza and Anthony M Reginato. "Calcium-Containing Crystal-Associated Arthropathies in the Elderly". In: *Federal Practitioner* (2016). URL: www.fedprac.com.

[17] Francesca Oliviero et al. "Prevalence of calcium pyrophosphate and monosodium urate crystals in synovial fluid of patients with previously diagnosed joint diseases". In: *Joint Bone Spine* 80 (2013), pp. 287–290. DOI: 10.1016/j.jbspin.2012.08.006. URL: www.sciencedirect.com.

[18] Adrian C Jones et al. *Diseases Associated With Calcium Pyrophosphate Deposition Disease*. Tech. rep. 1992.

[19] L Punzi et al. "Chondrocalcinosis is a feature of Gitelman's variant of Bartter's syndrome. A new look at the hypomagnesemia associated with calcium pyrophosphate dihydrate crystal deposition disease - PubMed". In: *Rev Rhum Engl Ed* 65.10 (1998), pp. 571–4. URL: https://pubmed.ncbi.nlm.nih.gov/9809361/.

[20] Pascal Richette, Thomas Bardin, and Michael Doherty. "An update on the epidemiology of calcium pyrophosphate dihydrate crystal deposition disease". In: (). DOI: 10.1093/rheumatology/kep081. URL: https://academic.oup.com/rheumatology/article/48/7/711/1789541.

[21] Sebastian E Sattui, Jasvinder A Singh, and Angelo L Gaffo. "COMORBIDITIES IN PATIENTS WITH CRYSTAL DISEASES AND HYPERURICEMIA". In: *Rheumatic Disease Clinics of North America* 201.2 (2014), pp. 251–278. DOI: 10.1016/j.rdc.2014.01.005.

[22] Angela Swan et al. *Evidence for a causal relationship between the structure, size, and load of calcium pyrophosphate dihydrate crystals, and attacks of pseudogout*. Tech. rep. 1995, pp. 825–830.

[23] C. I. Winternitz, J. K. Jackson, and H. M. Burt. "The interaction of monoclinic calcium pyrophosphate dihydrate crystals with neutrophils". In: *Rheumatology International* 16.3 (1996), pp. 101–107. ISSN: 01728172. DOI: 10.1007/BF01409981.

[24] D. Berendsen et al. "Crystal identification of synovial fluid aspiration by polarized light microscopy. An online test suggesting that our traditional rheumatologic competence needs renewed attention and training". In: *Clinical Rheumatology* 36.3 (2017), pp. 641–647. ISSN: 14349949. DOI: 10.1007/s10067-016-3461-0.

[25] Shumaila M Iqbal et al. "Updated Treatment for Calcium Pyrophosphate Deposition Disease: An Insight". In: *Cureus* 11.1 (2019). DOI: 10.7759/cureus.3840.

[26] Xinhui Duan et al. “Differentiation of Calcium Oxalate Monohydrate and Calcium Oxalate Dihydrate Stones Using Quantitative Morphological Information from Micro-Computerized and Clinical Computerized Tomography NIH Public Access”. In: *J Urol* 189.6 (2013), pp. 2350–2356. DOI: 10.1016/j.juro.2012.11.004.

[27] Elizabeth C Lorenz et al. “Update on Oxalate Crystal Disease”. In: *Curr Rheumatol Rep* 15.7 (2013), p. 340. DOI: 10.1007/s11926-013-0340-4.

[28] Gianantonio Saviola et al. “Can clodronate be effective in the treatment of disabling hydroxyapatite crystal-deposition disease? A report of two cases”. In: *Rheumatology International* 31.3 (2010), pp. 415–417. DOI: 10.1007/s00296-010-1575-2Ãŕ. URL: https://hal.archives-ouvertes.fr/hal-00612023.

[29] Hiroyuki Kuroda et al. *A Case of Probable Hydroxyapatite Deposition Disease (HADD) of the Hip*. Tech. rep. 3. 2004, pp. 141–144.

[30] P Hongsmatip et al. “Calcium hydroxyapatite deposition disease: Imaging features and presentations mimicking other pathologies”. In: *European Journal of Radiology* 120.April (2019), p. 108653. ISSN: 18727727. DOI: 10.1016/j.ejrad.2019.108653.

[31] O Azmat and P P Nagtode. “” Hydroxyapatite Crystal Deposition Disease ” An In- depth Analysis to Improve Understanding and Facilitate Symptomatic Relief”. In: *European Society of Muscoskeletal Radiology* (2015), pp. 1–29.

[32] Chengcheng Jin et al. “NLRP3 inflammasome plays a critical role in the pathogenesis of hydroxyapatite-associated arthropathy”. In: *Proceedings of the National Academy of Sciences of the United States of America* 108.36 (Sept. 2011), pp. 14867–14872. ISSN: 00278424. DOI: 10.1073/pnas.1111101108.

[33] Reddy Ravikanth et al. “Hydroxyapatite Crystal Deposition Disease of the Shoulder: A Review of Cases and Literature”. In: *J Recent Surg Med Sci* 4 (2018), pp. 43–46. ISSN: 2455-7420. DOI: 10.1055/s-0038-1676663.

[34] M.B. Lazarevic et al. “Cholesterol Crystals in Synolvial and bursal fluid”. In: *Seminars in Arthritis and Theumatism* 23.2 (1993), pp. 99–103.

[35] K Im et al. *Images in Clinical Medicine Cholesterol Crystals*. Tech. rep. 2020.

[36] H Gur and M Ehrenfeld. *The Benign Long Crystal Term Effect of Cholesterol Synovial Cysts*. Tech. rep. 3. 1994.

[37] J Dylewski, Z Awan, and I Roy. “Acute monoarticular arthritis caused by Maltese cross-like crystals”. In: *Canedian Medical Association* 172.6 (2005), pp. 741–742. DOI: 10.1503/cmaj.045248.

[38] S.E. Jacob et al. “Acute Monoarticular Maltese Cross – like Crystal Associated”. In: *Acta Cytologica* (2010).

[39] B Li et al. “Chemical characterization of Maltese-cross birefringent particles in synovial fluid samples collected from symptomatic joints.” In: *Joint Bone Spine* 85 (2018), pp. 501–503. DOI: https://doi.org/10.1016/j.jbspin.2017.09.004.

[40] P.J. Cornbleet and S.W Judkins. “Synovial fluid crystal analysis”. In: *Laboratory Medicine* 28.12 (1997), pp. 774–779.

[41] Porter Young and Kelly C Homlar. “A Case Report & Literature Review Extreme Postinjection Flare in Response to Intra-Articular Triamcinolone Acetonide (Kenalog)”. In: *The American Journal of Orthopedics* (2016). URL: www.amjorthopedics.com.

[42] Charles B. Kahn, Joseph L. Hollander, and H. Ralph Schumacher. “Corticosteroid Crystals in Synovial Fluid”. In: *JAMA: The Journal of the American Medical Association* 211.5 (22 1970), pp. 807–809. ISSN: 15383598. DOI: 10.1001/jama.1970.03170050041009.

[43] P Courtney and M Doherty. “Joint aspiration and injection and synovial fluid analysis”. In: *Best Practice & Research Clinical Rheumathology* 23 (2009).

[44] D.B Murphy et al. *Principles of Birefringence — MicroscopyU (en-US)*. URL: https://www.microscopyu.com/techniques/polarized-light/principles-of-birefringence (visited on 05/07/2020).

[45] Yibo Zhang et al. “Wide-field imaging of birefringent synovial fluid crystals using lens-free polarized microscopy for gout diagnosis OPEN”. In: *Scientific Reports* (2016). DOI: 10.1038/srep28793. URL: www.nature.com/scientificreports/.

[46] D. D. Le Pevelen. “NIR FT-raman”. In: *Encyclopedia of Spectroscopy and Spectrometry*. Elsevier, Jan. 2016, pp. 98–109. ISBN: 9780128032244. DOI: 10.1016/B978-0-12-409547-2.12150-X.

[47] Y Liu and H Gao. *Raman: Theory*. 2020. (Visited on 09/30/2020).

[48] M.L Frezzotti, F Tecce, and A Casagli. “Raman spectroscopy for fluid inclusion analysis”. In: *Journal of Geochemical Exploration* 112 (2012), pp. 1–20.

[49] Xingguo Cheng et al. *Analysis of Crystals Leading to Joint Arthropathies by Raman Spectroscopy: Comparison with Compensated Polarized Imaging*. Tech. rep. 2009.

[50] Declan J. Curran, Laurence Rubin, and Mark R. Towler. “Raman spectroscopy applied to the noninvasive detection of monosodium urate crystal deposits”. In: *Clinical Medicine Insights: Arthritis and Musculoskeletal Disorders* 8 (2015), pp. 55–58. ISSN: 11795441. DOI: 10.4137/CMAMD.S29061.

[51] Corina D. Hosu et al. *Raman spectroscopy applications in rheumatology*. June 2019. DOI: 10.1007/s10103-019-02719-2.

[52] Bolan Li, Shan Yang, and Ozan Akkus. “A Customized Raman System for Point-of-Care Detection of Arthropathic Crystals in the Synovial Fluid”. In: *Analyst* 139.4 (2013), pp. 823–830. DOI: 10.1039/c3an02062b.

[53] Bolan Li et al. “A Point-of-Care Raman Spectroscopy–Based Device for the Diagnosis of Gout and Pseudogout”. In: *Arthritis and Rheumatology* 68.7 (2016), pp. 1751–1757. ISSN: 23265205. DOI: 10.1002/art.39638.

[54] Martin Fuerst et al. “Investigation of calcium crystals in OA knees”. In: *Rheumatol Int* 30 (2010), pp. 623–631. DOI: 10.1007/s00296-009-1032-2.

[55] Howell G.M. Edwards et al. “FT-Raman spectroscopy of lichens on dolomitic rocks: An assessment of metal oxalate formation”. In: *Analyst* 128.10 (2003), pp. 1218–1221. ISSN: 00032654. DOI: 10.1039/b306991p.

[56] Gema Cabello et al. “Cu@Au self-assembled nanoparticles as SERS-active substrates for (bio)molecular sensing”. In: *Journal of Alloys and Compounds* 791.March (2019), pp. 184–192. ISSN: 09258388. DOI: 10.1016/j.jallcom.2019.03.279.

[57] Jessica A. Stammeier et al. “In-situ Raman spectroscopy of amorphous calcium phosphate to crystalline hydroxyapatite transformation”. In: *MethodsX* 5 (Jan. 2018), pp. 1241–1250. ISSN: 22150161. DOI: 10.1016/j.mex.2018.09.015.

[58] K. Tesar et al. “Raman scattering yields cubic crystal grain orientation”. In: *Scientific Reports* 9.1 (Dec. 2019), pp. 1–8. ISSN: 20452322. DOI: 10.1038/s41598-019-45782-z.

[59] Brighton De Jong. “Diagnosis of Gout and Pseudogout with Raman Spectroscopy Bachelor thesis”. In: (2019).

[60] F C Donnelly et al. “Synthesis of CaCO 3 nano-and micro-particles by dry ice carbonation”. In: *Chem. Commun* 53 (2017), p. 6657. DOI: 10.1039/c7cc01420a.

[61] William J.B. Dufresne, Carson J. Rufledt, and Craig P. Marshall. “Raman spectroscopy of the eight natural carbonate minerals of calcite structure”. In: *Journal of Raman Spectroscopy* 49.12 (Dec. 2018), pp. 1999–2007. ISSN: 0377-0486. DOI: 10.1002/jrs.5481.

[62] B Liszka. “New technology to investigate crystallization on polymer surfaces”. PhD thesis. Enschede, The Netherlands: University of Twente, May 2016. ISBN: 9789036541169. DOI: 10.3990/1.9789036541169.

[63] J Yu et al. “Calcium content of different compositions of gallstones and pathogenesis of calcium carbonate gallstones”. In: *Asian journal of Surgery* 36 (2013), pp. 26–35.

[64] G.B Ramírez-Rodríguez, J.M Delgado-López, and J Gómez-Morales. “Evolution of calcium phosphate precipitation in hanging drop vapor diffusion by in situ Raman microspectroscopy”. In: *CrystEngComm* 15 (2013), p. 2206. ISSN: 2165-2338. DOI: 10.1039/c2ce26556g. URL: www.rsc.org/crystengcomm.

[65] P. E. Timchenko et al. “Experimental studies of hydroxyapatite by Raman spectroscopy”. In: *Journal of Optical Technology* 85.3 (Mar. 2018), p. 130. ISSN: 1070-9762. DOI: 10.1364/jot.85.000130.

Appendices

A Signal from birefringent objects

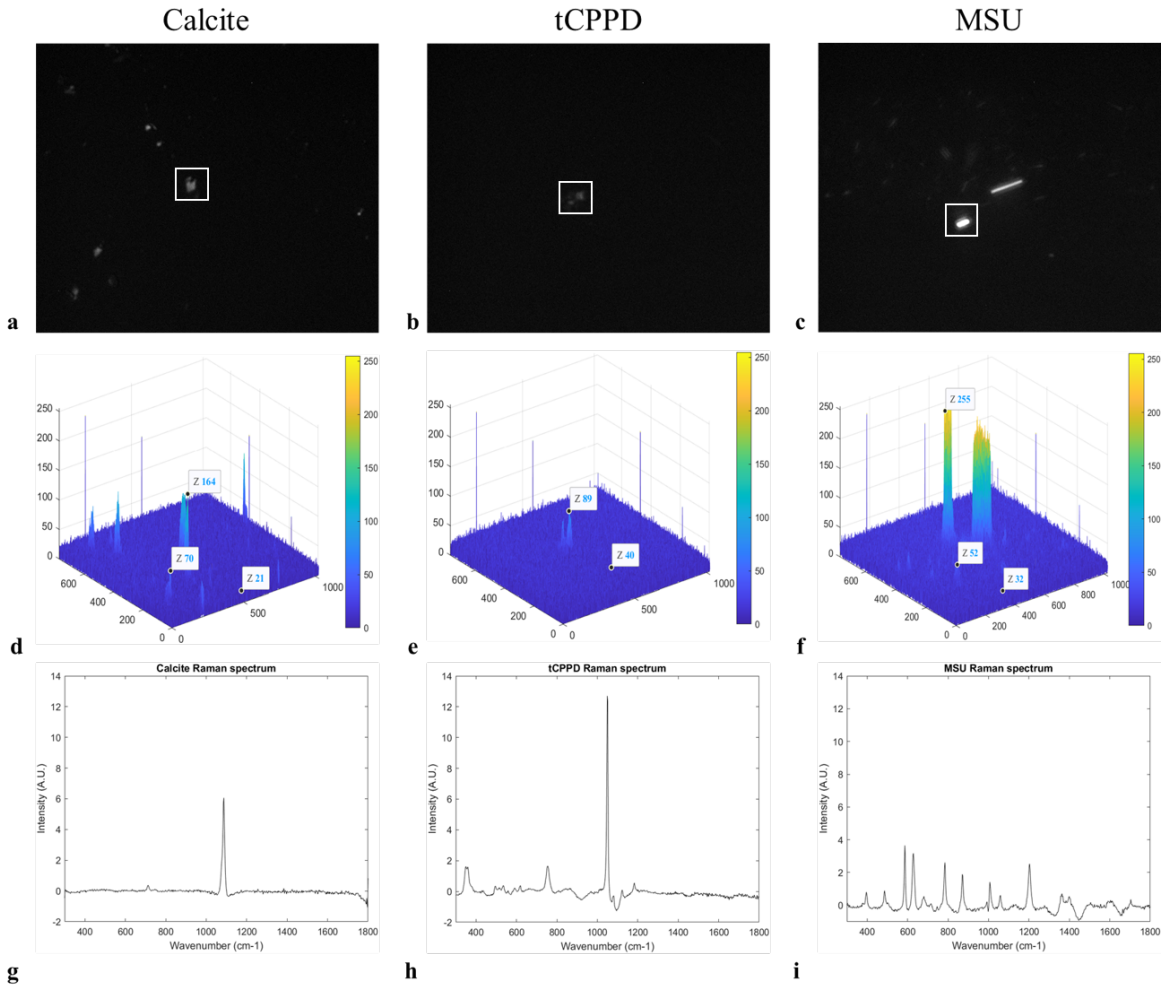

Figure 14: Grey scale images from different objects. a,b,c) brightfield images from Clacite, tCPPD and MSU respectively with brightfield imaging with polarizing filters placed perpendicular to each other to achieve a dark spot. d,e,f) grey scale images from the same crystals with different intensity levels. g,e,f Raman spectra of the objects indicated by the white square in a,b and c

B Raman spectra in the database

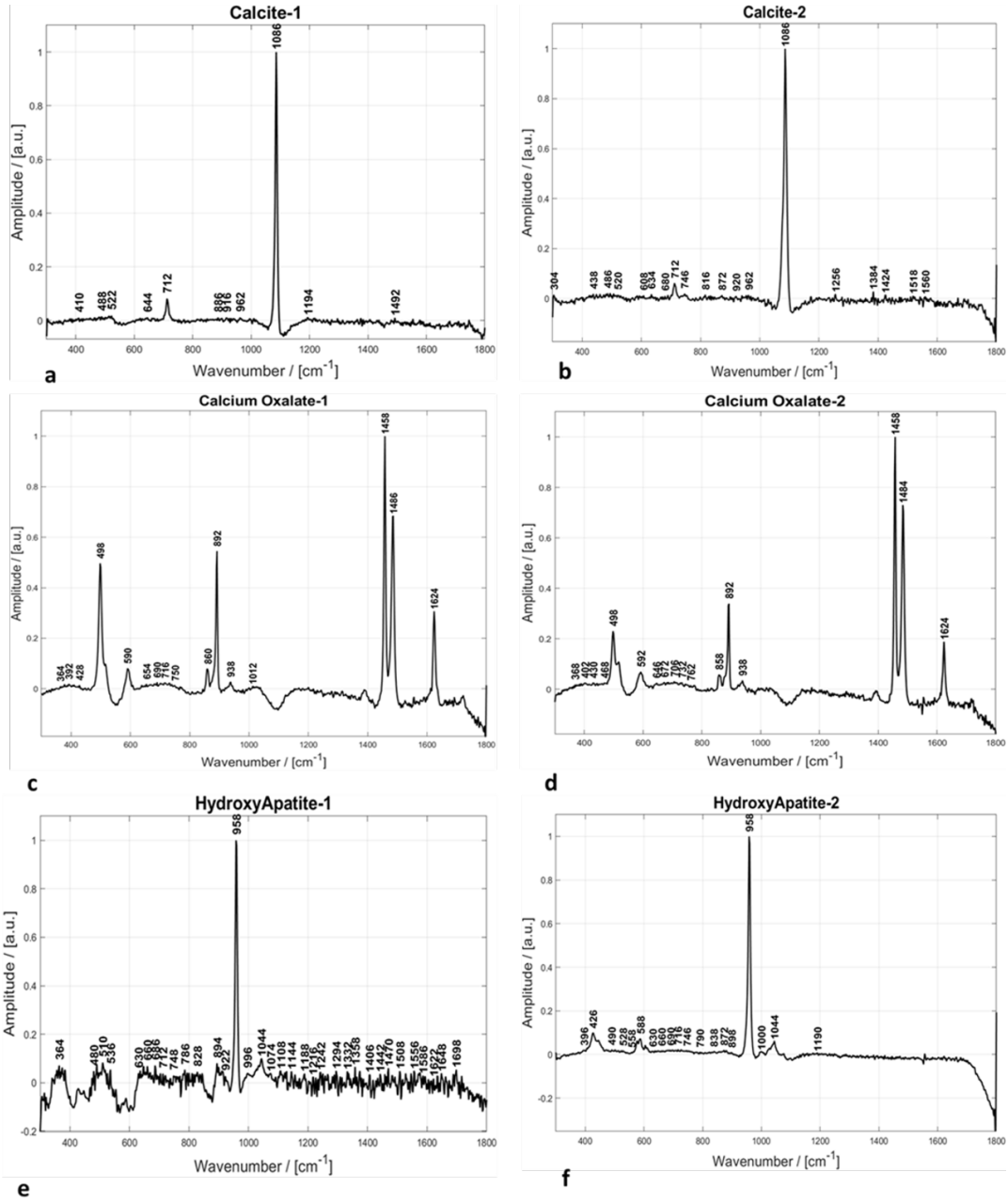

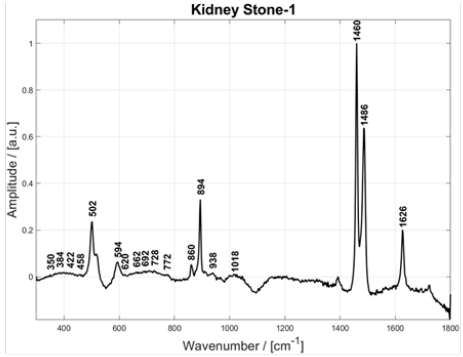
Kidney Stone-1
Amplitude / [a.u.]
Wavenumber / [cm-1]
1460
1486
894
502
1626
860
938
1018
772
662
692
720
894
620
350
394
432
458

g

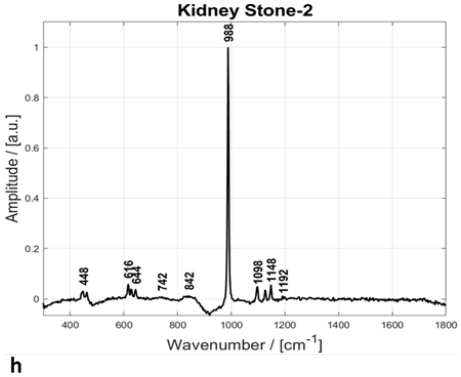
Kidney Stone-2
Amplitude / [a.u.]
Wavenumber / [cm-1]
988
448
616
644
742
842
1098
1148
1192

h

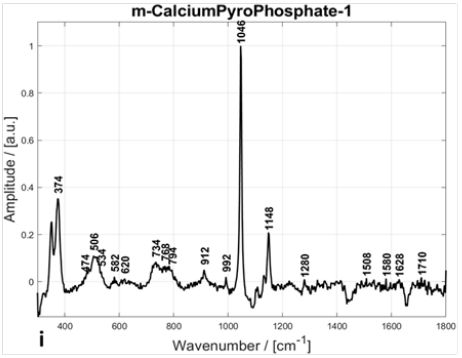
m-CalciumPyroPhosphate-1
Amplitude / [a.u.]
Wavenumber / [cm-1]
1046
374
506
474
534
582
620
734
768
794
912
992
1148
1280
1508
1580
1628
1710

i

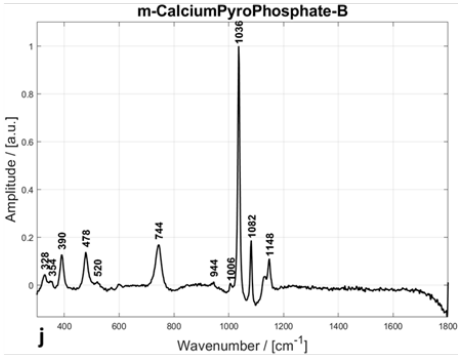
m-CalciumPyroPhosphate-B
Amplitude / [a.u.]
Wavenumber / [cm-1]
1036
328
352
390
478
520
744
944
1006
1082
1148

j

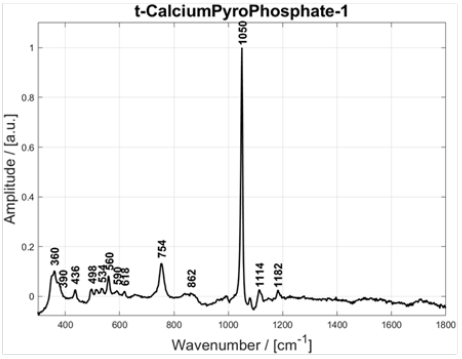
t-CalciumPyroPhosphate-1
Amplitude / [a.u.]
Wavenumber / [cm-1]
1050
360
390
436
498
534
560
596
678
754
862
1114
1182

k

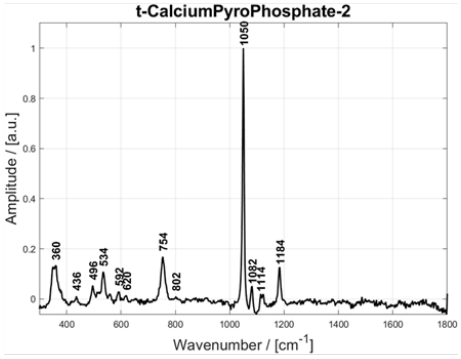
t-CalciumPyroPhosphate-2
Amplitude / [a.u.]
Wavenumber / [cm-1]
1050
360
436
496
534
592
620
754
802
1082
1114
1184

l

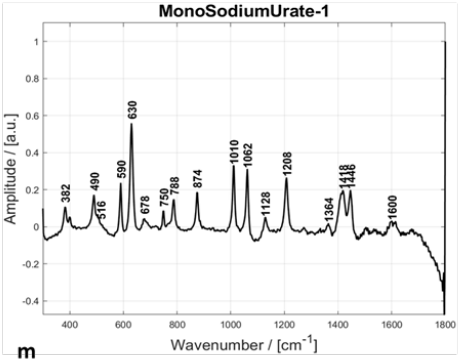
MonoSodiumUrate-1
Amplitude / [a.u.]
Wavenumber / [cm-1]
630
382
490
516
590
678
750
788
874
1010
1062
1128
1208
1364
1418
1448
1600

m

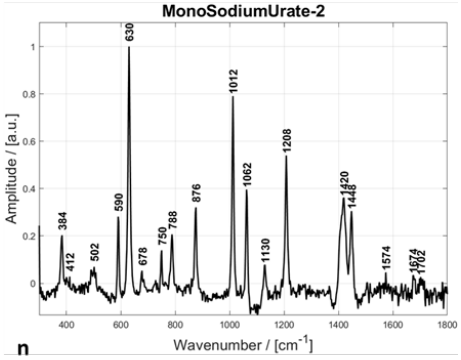
MonoSodiumUrate-2
Amplitude / [a.u.]
Wavenumber / [cm-1]
630
1012
1208
384
412
502
590
678
750
788
876
1062
1130
1420
1448
1574
1674
1702

n

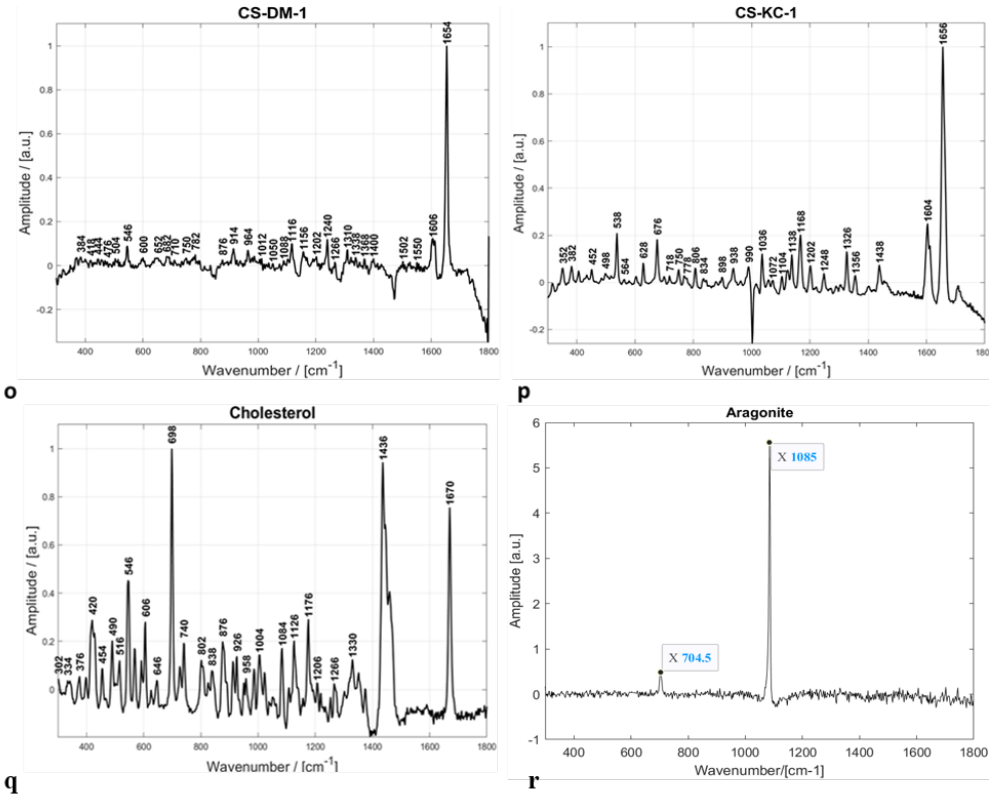

Figure 15: All Raman spectra that were placed in the database. a,b) Presumed calcite. c,d) Calcium oxalate. e,f) Hydroxyapatite. g,h) Spectra form kidney stones. i) m-CPPD. j) m-CPPT β. k,l) t-CPPD. m,n) MSU. o) Corticosteroid DepoMedrol. p) Kenacort. q) Cholesterol. r) Aragonite.

C Correlation of MSU Raman spectra

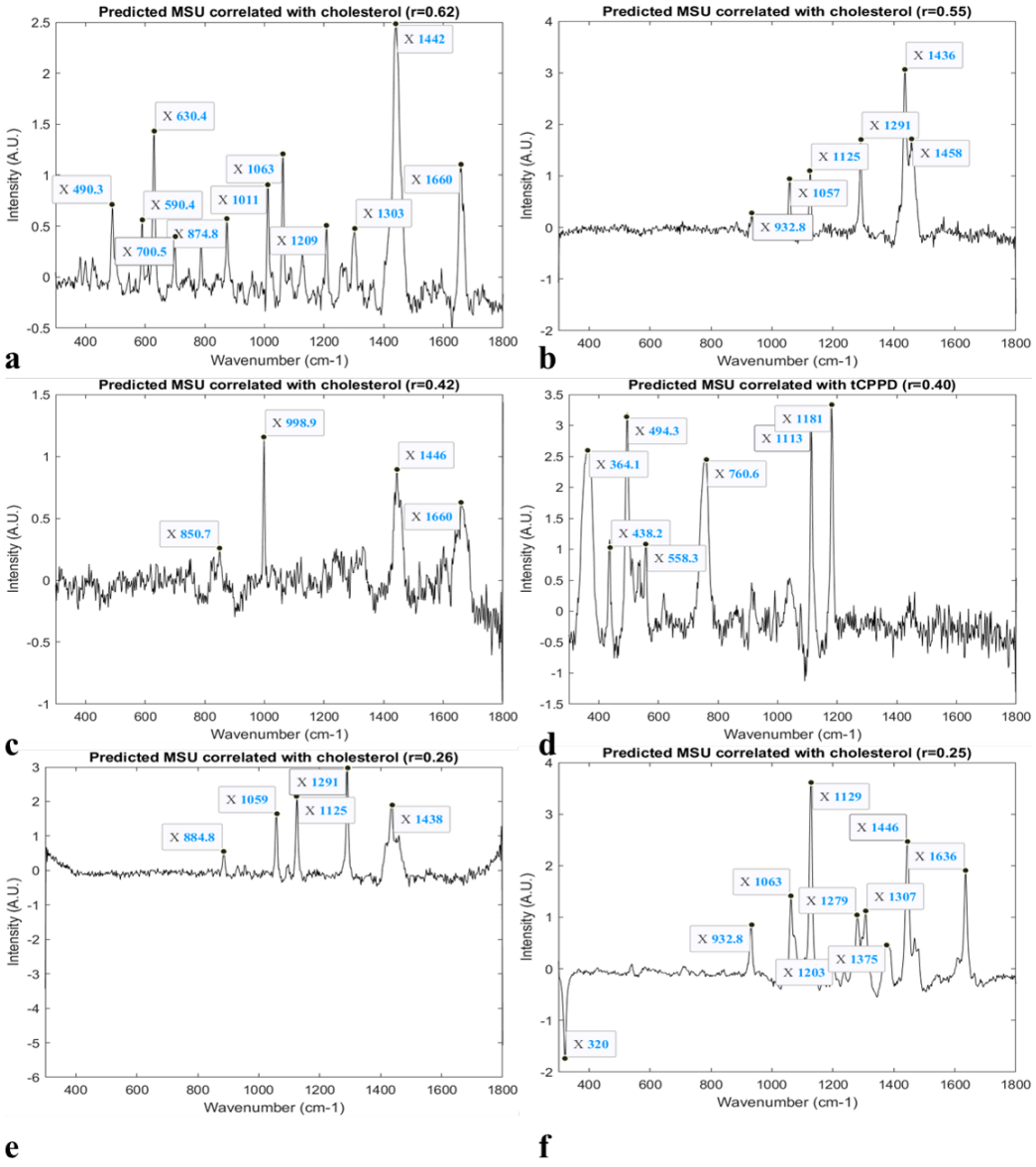

Figure 16: Raman spectra from measurements that where predicted to be MSU but correlated with other database components

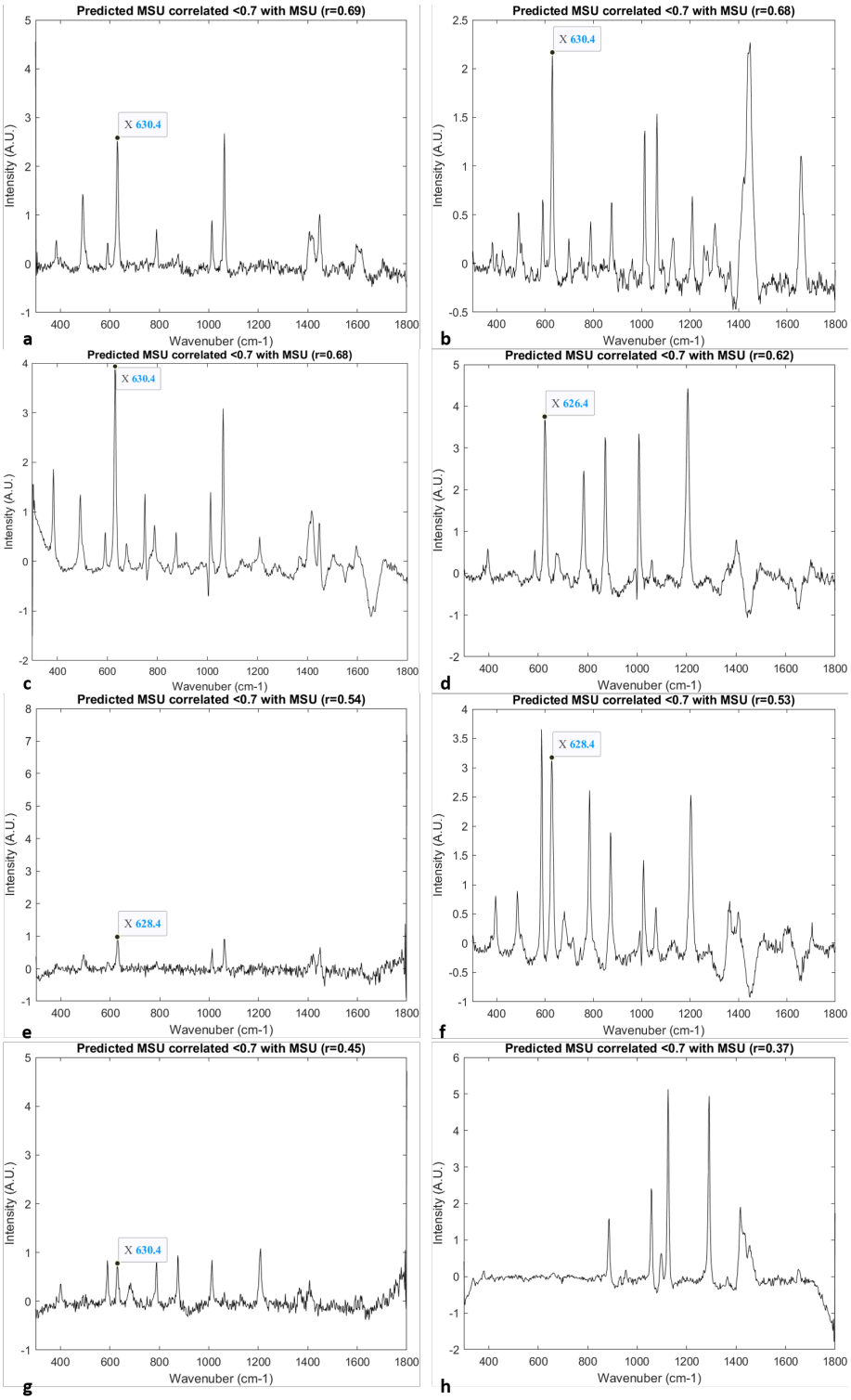

Figure 17: Raman spectra from measurements that where predicted to be MSU and correlated with MSU with a correlation coefficient lower than 0.6

D Correlation of CPPD Raman spectra

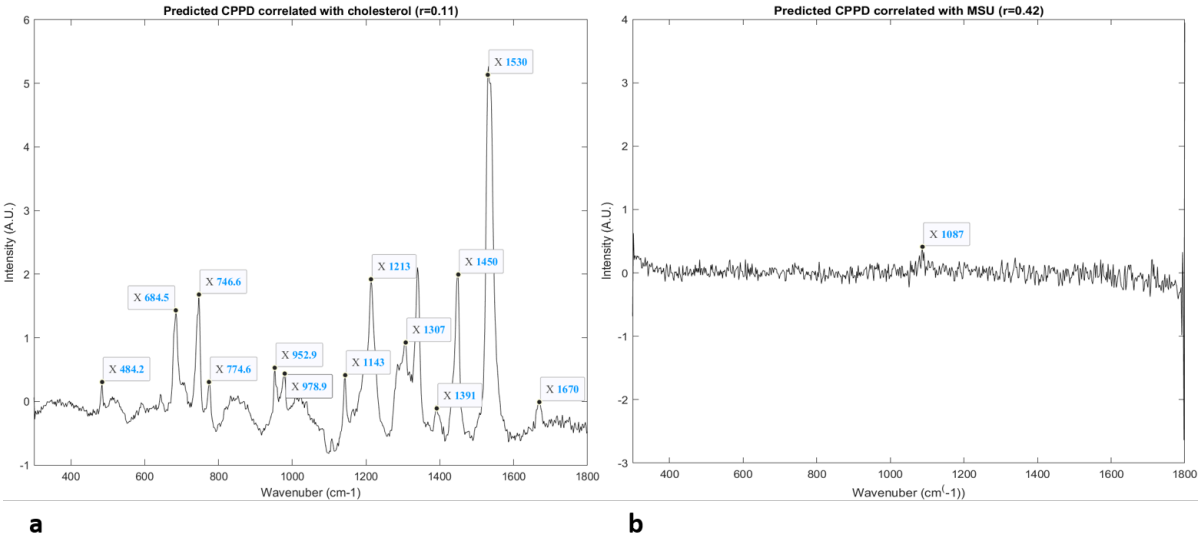

Figure 18: Raman spectra from measurements that where predicted to be CPPD but correlated with another database component

E Correlation of unknown components

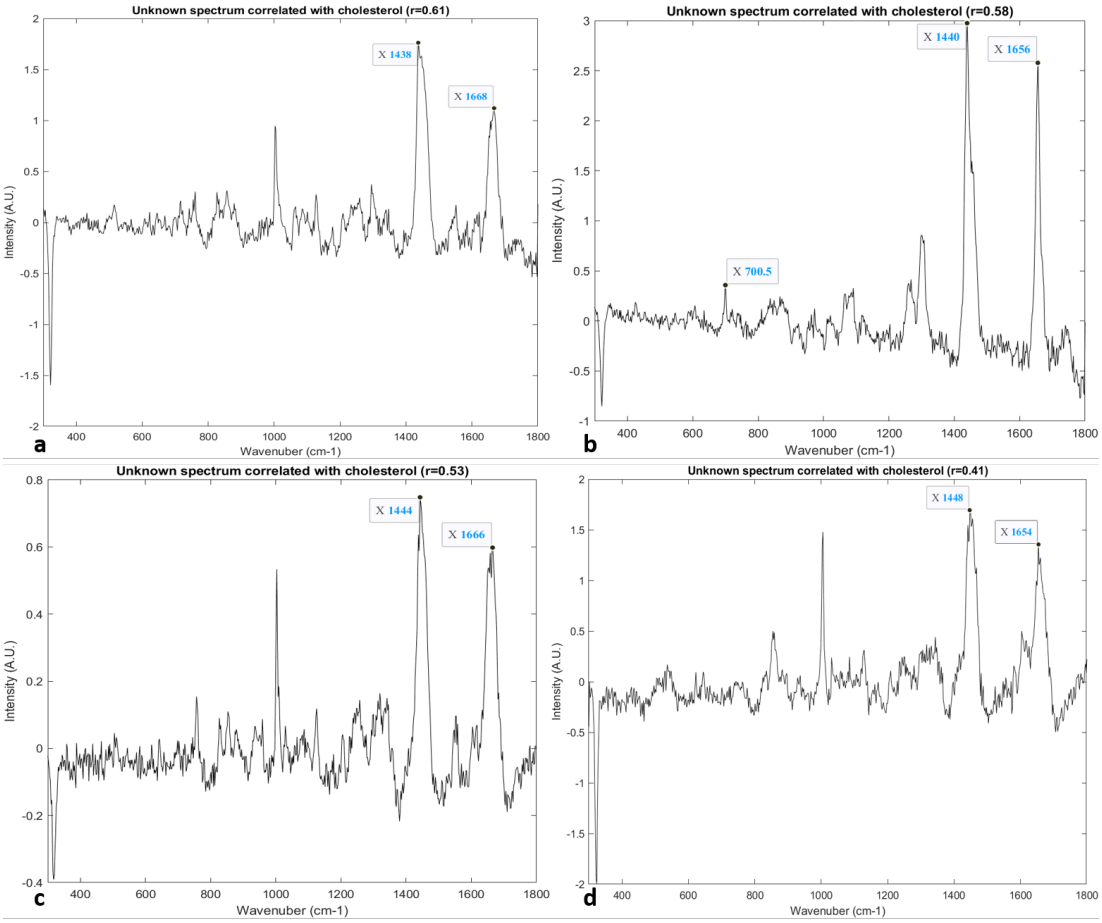

Figure 19: Unknown Raman spectra that correlated with cholesterol with different correlation strengths

F Detection of new crystals

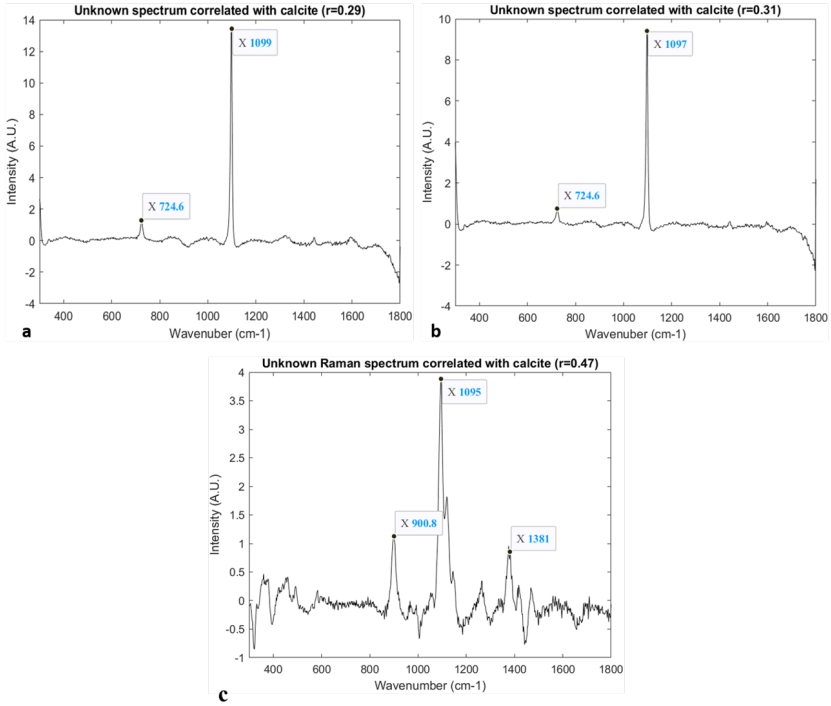

Figure 20: Unknown Raman spectra that correlated with calcite with different correlation strengths

G Correlation of synthetic crystals

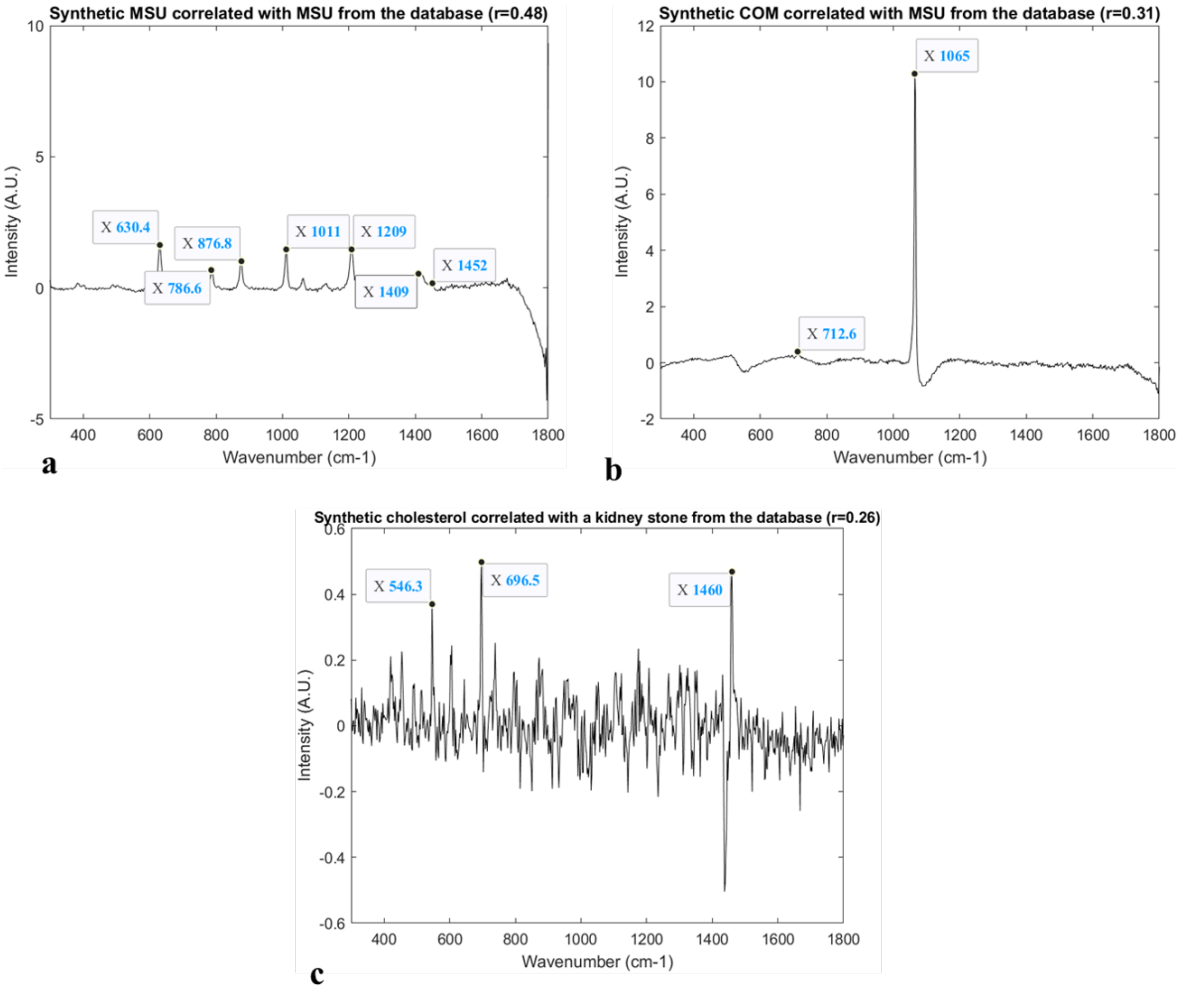

Figure 21: Synthetic crystals that correlated with different database components or correlated poorly. a) Synthetic MSU correlating poorly with MSU. Characteristic MSU peaks are present. b) Synthetic calcium oxalate monohydrate correlating poorly with MSU. Peaks are similar to calcite Raman spectrum. c) Synthetic cholesterol correlating with one of the kidney stone Raman spectra from the database.

H Patient samples

Table 5: All patient samples with indications obtained from Rheumatologists and Raman spectra that where found in the samples

Sample number	Indication from Rheumatologist	Times measured	Found with Raman	Correlated with database	Correlation
1	MSU	3	MSU	MSU	0.84
				MSU	0.97
				MSU	0.83
2	MSU	3	Unknown Raman spectrum	Cholesterol	0.55
				Cholesterol	0.26
				MSU	0.37
3	MSU	4	MSU	MSU	0.79
				MSU	0.85
				MSU	0.68
				Cholesterol	0.62
4	MSU	4	MSU, calcite	Calcite	0.78
				MSU	0.78
				MSU	0.62
				MSU	0.53
5	MSU	5	Two unknown Raman spectra	Cholesterol	0.42
				Cholesterol	0.41
				Cholesterol	0.55
				DepoMedrol	0.36
				Calcite	0.62
6	MSU	6	Hydroxyapatite, aragonite	Hydroxyapatite	0.75
				Hydroxyapatite	0.77
				Aragonite	0.90
				Aragonite	0.90
				Aragonite	0.93
				Cholesterol	0.18
7	CPPD	6	Calcite	Calcite	0.93
				Calcite	0.98
				Calcite	0.93
				Calcite	0.95
				MSU	0.11
				Cholesterol	0.11
8	CPPD	6	Aragonite	Aragonite	0.93
				Aragonite	0.98
				Kidney stone	0.42
				Kidney stone	0.1
				Kidney stone	0.43
				Cholesterol	0.37
9	MSU, CPPD, KenaCort	8	t-CPPD, calcium oxalate monohydrate	t-CPPD	0.93
				t-CPPD	0.96
				t-CPPD	0.97
				t-CPPD	0.4
				Kidney stone	0.74
				m-CPPt-β	0.1
				Hydroxyapatite	0.19
				Hydroxyapatite	0.27
10	Kidney stone	4	Calcium oxalate monohydrate	Kidney stone	0.62
				Kidney stone	0.61
				Kidney stone	0.92
				Calcium oxalate monohydrate	0.83
11	Kidney stone	5	Calcium oxalate monohydrate	Aragonite	0.60
				Aragonite	0.51
				Kidney stone	0.92
				Calcium oxalate monohydrate	0.18

Continued on next page

Table 5 – continued from previous page

Sample number	Indication from Rheumatologist	Times measured	Found with Raman	Correlated with database	Correlation
				Calcium oxalate monohydrate	0.74
12	Maltese cross	3	Two unknown Raman spectra	Kidney stone	0.37
				Kidney stone	0.39
				Kidney stone	0.41
13	No crystals	0	No crystals		
14	Unknown	3	t-CPPD	t-CPPD	0.97
				Calcite	0.29
				Calcite	0.31
15	Unknown	1	MSU	MSU	0.88
16	Unknown	4	MSU	MSU	0.78
				MSU	0.83
				MSU	0.84
				MSU	0.62
17	Unknown	1	Unclear Raman spectra	Kidney stone	0.25
18	Unknown	7	Aragonite, m-CPPD	m-CPPD	0.82
				m-CPPD	0.81
				m-CPPD	0.79
				m-CPPD	0.73
				Aragonite	0.83
				Aragonite	0.81
				Aragonite	0.65
19	Unknown	1	Calcite	Calcite	0.71
20	Unknown	4	MSU	MSU	0.31
				MSU	0.41
				MSU	0.72
				MSU	0.73
21	Unknown	6	m-CPPD, t-CPPD, unknown spectrum	m-CPPD	0.87
				t-CPPD	0.87
				t-CPPD	0.96
				t-CPPD	0.96
				t-CPPD	0.97
				MSU	0.14
22	Unknown	5	t-CPPD, Kenacort	t-CPPD	0.9
				t-CPPD	0.98
				Kenacort	0.91
				Kenacort	0.95
				Kenacort	0.92